Université de Technologie de Compiègne

Génie Mécanique

Final Year Project

Theory and Simulation of Confined Active Suspensions

Adrien Lefauve

Supervisor:
Professor David Saintillan

January 21 – July 12, 2013

Abstract

The modeling of active suspensions, or suspensions of self-propelling particles such as swimming microorganisms remains a great challenge despite their ubiquity in biological systems. The long-ranged fluid-mediated interactions between suspended particles in the low-Reynolds-number regime are known to give rise to collective motion and large-scale spatiotemporal coherent patterns. The mechanisms behind the emergence of collective dynamics and self-organization from individual interactions has received increasing attention in the past few years, and could provide valuable insight into the behavior of nonequilibrium dissipative systems. In this work, we use theory and numerical simulation to study the behavior of confined active suspensions, with emphasis on fore-aft asymmetric swimmers.

Continuum kinetic theory and numerical simulations demonstrated that bulk suspensions of tail-actuated swimmers are subject to a generic long-wavelength instability, suggesting that systems larger than a threshold size are prone to mesoscale orientational order in the form of bend modes. However, according to recent evidence, the nature of hydrodynamic interactions radically changes under confinement between two rigid plates, a situation of particular relevance for bacterial swarms on rigid boundaries or in a thin wall-bounded film. The resulting interactions are weaker than in unconfined geometries and it is unknown whether they also give rise to collective motion.

By means of a stability analysis on a continuum kinetic model coupled to the Stokes flow equations, we extend existing linear theories and show that bulk suspensions of confined large-head swimmers experience a similar generic instability characterized by propagating large-scale polarized waves. The predicted features of this instability are then captured using direct particle simulations and linear results for the wavenumber dependence are compared. We then gain insight into the surprising long-time dynamics and pattern formation of large-heads and shed light on the underlying mechanisms. Nonlinear simulations further reveal that in spite of being linearly stable, suspensions of large-tail swimmers are also prone to a long-wavelength instability, driving fascinating quasi-periodic vortical motions above a critical system size. Finally, we show using a quasi-one-dimensional model that self-propelled organisms in a narrow channel subject to a stabilizing external flow obey a traffic flow equation. The predicted traffic jam behavior is then successfully observed in simulations and we explain why it contrasts with an apparently similar result recently reported in passive suspensions.

Acknowledgements

I would like to express my gratitude to Professor David Saintillan for giving me the opportunity to be part of his research group and work on an exciting topic. His support and guidance throughout this six-month internship have been of inestimable value. I am especially grateful for his help, patience and insightful discussions during long research meetings which greatly contributed to develop my curiosity and interest in theoretical work. Through advice and suggestions, he communicated me his passion for scientific research and I owe him the enthusiasm with which I completed this work.

I am also grateful to Barath Ezhilan, Harishankar Manikantan, Ku Da and Debasish Das, who contributed to make this research period a great and enjoyable experience. I benefited from valuable discussions, comments and encouragements and their commitment to research inspired me. Thanks to Ku Da for helping me with the contact algorithm, and to Barath, Debasish and Harishankar for tolerating the heat and noise from the servers while I was running countless simulations.

Finally, my thanks go to Dominique Bathès-Biesel and Anne-Virginie Salsac, who accepted to be part of my thesis commitee and offered me the opportunity to defend my work. They made this work rewarding and contributed to its quality.

Contents

Chapter 1

Introduction

This chapter starts with a brief introduction to the field of active suspensions and highlights the relevance of the following work in this context. We then proceed to present the model upon which this work relies for the description of dynamics of confined active suspensions.

1.1 Active suspensions

The omnipresence of microorganisms in the biosphere and their role in phenomena as fundamental as pathogenic infection, digestion, reproduction or CO_2 capture and mixing in the oceans motivates the understanding of their behavior [1]. In the past decades, efforts have been made to understand the swimming mechanisms of microorganisms, which, unlike most familiar macroscopic organisms, evolve in viscous fluid environments where inertia is negligible. In this low-Reynolds-number world, the disturbance flow created by a moving particle has often a slow spatial decay, which allows for strong fluid-mediated interactions with other neighboring particles in large colonies. These so called *living fluids* or *active suspensions*, referring to the active energy input from their suspended microstructure, have attracted many scientific communities, from biology and physics to engineering and applied mathematics [2]. The fascinating phenomena that have already been studied include enhanced tracer diffusion and swimming speeds, large-scale chaotic and vortical flows and giant density fluctuations, even in absence of external forcing. Since such unusual and complex fluid motions are typical of high-Reynolds-number turbulence, they are often referred to as *bacterial turbulence*.

Among several theoretical frameworks proposed to elucidate the underlying mechanisms, the simple kinetic model developed by Saintillan and Shelley [3, 4], based on a continuous probability distribution function coupled with the Stokes equation, has proven particularly successful in understanding various phenomena that we will outline next. Their first study addressed the stability of a three dimensional homogeneous suspension and revealed that isotropic suspensions of tail-actuated swimmers[1] were unstable to long-wavelength perturbations. Specifically, this suggests that instability may occur in systems whose

[1] This common type of swimmers achieve swimming by pushing at the rear of their body and are commonly refered to as *pushers*, as opposed to head-actuated organisms called *pullers*.

linear size exceeds a given threshold inversely proportional to the swimmers' concentration [3, 4]. This behavior has then been successfully captured in numerical simulations, based on the integration of the distribution function coupled with the fluid flow [3, 4] as well as slender body theory [5] and insight into nonlinearities has been gained, showing long-time dynamics characterized by strong concentration fluctuations, enhanced mixing as well as quasi-periodic formation and break-down of complex structures. To account for the existence of background flows commonly observed in Nature, further theory and simulations by Alizadeh Pahlavan and Saintillan suggested that an external shear flow has a stabilizing effect on the suspension by controlling the orientation of particles [7]. Saintillan then extended this model to analyze the effective rheology of active suspensions [8, 9], where pushers have been surprisingly found to decrease the effective fluid viscosity, confirming experimental findings [10]. Chemotaxis, or the interaction of microorganisms with chemical fields (such as in a thin film of bacterial suspension surrounded by oxygen) has also been studied by coupling the previous model to the oxygen field and modeling faithfully the complex response of individual bacteria to oxygen concentrations. Simulations by Ezhilan, Alizadeh Pahlavan and Saintillan [11] confirmed observations [12] of a transition from 2D behavior to 3D chaotic patterns as the film thickness increases, significantly enhancing oxygen mixing from free surfaces to the bulk of the film, with obvious benefits to the bacteria. Eventually, an extension of this kinetic model has been recently used both theoretically and numerically by Ezhilan, Shelley and Saintillan [13] to investigate the stability and nonlinear dynamics of semi-concentrated suspensions, taking into account steric interactions and reporting novel dynamics experimentally reported in dense bacterial swarms [14].

Whereas these efforts to extend the original model were successful in the fundamental understanding of various phenomena, improvements to capture even more complex effects will be needed to quantitatively account for many experimental results [1]. Among other interests, the effects of high bacterial concentrations are regarded as particularly challenging for a continuum model, as well as unsteady swimming actuation, which has until then been neglected despite evidence of its significant effects [15]. Eventually, increasing interest is shown for the influence of confinement. By assuming periodic boundary conditions, most calculations and simulations capture the bulk behavior without examining the dominant and dramatic effect that boundaries might have in confined geometries. The following work is precisely aimed at gaining insight into the effect of rigid boundaries on the stability and nonlinear dynamics of quasi-2D suspensions of self-propelled organisms. Confined suspensions have been studied in the past few years, mainly in the context of droplet emulsions (see a review by Beatus, Bar-Ziv and Tlusty [16]), which although they are not self-propelled particles, share similarities with active suspensions. In this respect, results including the propagation of Burgers shock waves explained as a genuine effect of confinement of advected droplets [17, 18, 19] are encouraging. More generally, the study of 2D suspensions seems very promising to gain insight into the complex dynamics leading to collective phenomena and pattern formation in non-equilibrium systems, where governing principles are still puzzling theorists [16]. Active suspensions are a good example of dissipative many-body systems with strong interactions, which are omnipresent in Nature. Moreover, they exhibit rich phenomena while being theoretically tractable owing to the linearity of the viscous flow equations. As we shall see, some theoretical difficulties are further avoided by the two-dimensionality of confined suspensions, which makes them exceptionally well-suited

to study the basic principles of many-body physics with long-ranged interactions [16].

In this perspective, this work hopes to elucidate some features of the dynamics of self-propelled particles lacking fore-aft symmetry, as a general model for biological swimmers, embedded in strongly and rigidly confined geometries such as in a thin gap between two plates. We will make use of a combination of theory and numerical simulation and will heavily rely on the kinetic model mentionned above and on a recent theoretical model for the interactions and mobility of confined swimmers by Brotto *et al.* [20].

1.2 Hydrodynamic interactions in confined geometries

In this section, we recall the basics of the disturbance Stokes flow generated by a typical biological swimmer in unconfined geometries and show how interactions are modified in a thin wall-bounded film, where the film thickness h is comparable with the particle height.

In the low-Reynolds-numbers realm, microorganisms exhibit numerous swimming strategies which have in common to rely on non-reciprocal shape deformation, as required by the Purcell scallop theorem [21]. Fig. 1.1 shows how microorganisms exert a net thrust $\mathbf{F}_p$ on the surrounding fluid, actuating their flagella in a non-reciprocal fashion. As gravitational effects are neglected (fluid and swimmer densities are often similar), an equal and opposite drag $\mathbf{F}_d = -\mathbf{F}_p$ must be exerted, typically distributed on parts of the body which do not contribute to propulsion [1]. As the application points of these forces are separated by a finite distance (about the organism size) the effect on the fluid is essentially that of a force dipole, whose sign differs for tail-actuated organisms, called *pushers* (Fig. 1.1a) and head-actuated ones, or *pullers* (Fig. 1.1b) [1]. Approximating the disturbance flow resulting from the complex force

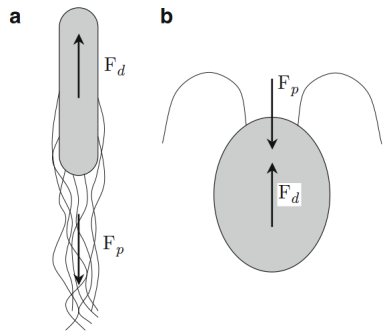

FIG. 1.1: Self-propulsion of (a) a tail-actuated microorganism (e.g. a bacterium) (b) a head-actuated microorganism (e.g. a microalga). These mechanisms result in force dipoles of opposite sign. Adapted from [1].

distribution on the swimmer as a force dipole singularity (or Stokes doublet) with $1/r^2$ spatial decay significantly simplifies the mobility problem but only holds in the limit of large inter-particle distance compared to the particle size [22]. This constitutes the first reason why such models heavily rely on the assumption that the suspension is *dilute*. As a swimmer moves through the fluid, it not only perturbs momentum density, but also mass density as a result of non-penetration at its boundaries. In the dilute limit, this perturbation is well approximated by a source dipole (also called source doublet or potential

dipole), with spatial decay in $1/r^3$, a higher-order contribution which we therefore neglect. Fig. 1.2 shows the differences between the flow induced by a force dipole (Fig. 1.2a) and a source dipole (Fig. 1.2b). As the hydrodynamic interactions decay with an exponent of two, less than the dimensionality of the system, unconfined suspensions fall into the category of systems with *strong long-ranged interactions*.

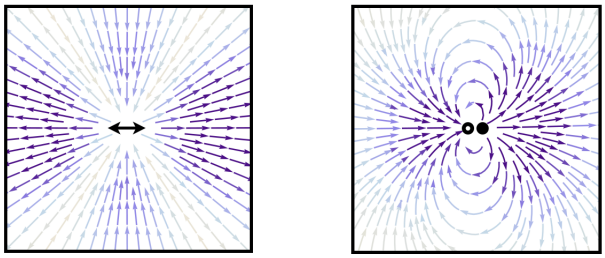

(*a*) (*b*)

FIG. 1.2: Streamlines due to (a) a 3D force dipole (Stokes doublet), which decays as $1/r^2$ (b) a 3D source doublet (potential dipole), which decays as $1/r^3$. Arrow length indicates flow intensity. Adapted from [23].

By constrast, quasi-2D systems are characterized by two rigid parallel boundaries breaking the translational symmetry of the fluid along the normal direction z, and transverse momentum can no longer be conserved. This leak can be seen in the no-slip boundary condition at the plates, resulting in a Poiseuille flow with finite momentum flux $\partial\mathbf{u}/\partial z$ into the confining surfaces [22]. It has been shown that fluid flow components normal to the plates resulting from a force monopole (Stokeslet) parallel to them decay exponentially in r/h (i.e. transverse momentum is not conserved over distances larger that h), and that the far field behavior was that of a 2D source dipole in the (x, y) plane [24]. Applied to the confined Stokes doublet from a self-propelled organism, this suggests a far-field that looks like a potential quadrupole with $1/r^3$ spatial decay. In contrast with momentum, since non-penetration at the boundaries must still hold, mass is obviously conserved under confinement. The source dipole term introduced in 3D to account for the finite size of swimmers is therefore still relevant. In the dilute limite, and when the film thickness is about the particle size, we neglect 3D effects due to the finite height of the particles and regard the flow as being essentially 2D. Far from a particle, the parabolic Poiseuille flow variables may thus be described by their averages on the (x, y) plane, and we use the classical result that the velocity is potential [25]:

$$\mathbf{u}(\mathbf{r}) = -\frac{h^2}{12\eta}\nabla\Pi(\mathbf{r}), \tag{1.1}$$

where $\Pi(\mathbf{r})$ is the pressure at $\mathbf{r} = (x, y)$ and η the dynamic viscosity. Specifically, the 2D source dipole term that we seek is the solution of Eq. (1.1) and the modified incompressibility relation [20]

$$\nabla \cdot \mathbf{u}(\mathbf{r}) = -\boldsymbol{\sigma} \cdot \nabla\delta(\mathbf{r} - \mathbf{R}(t)), \tag{1.2}$$

for a swimmer at $\mathbf{R}(t)$ with dipole moment $\boldsymbol{\sigma} = \sigma[\dot{\mathbf{R}}(t) - \mathbf{u}(\mathbf{R}(t))]$ resulting from the relative velocity of the swimmer with the background flow. Here σ scales as the particle area, $\mathbf{u}$ is the velocity in absence of the particle and δ the delta Dirac function. This is solved by [20]

$$\mathbf{u}^d(\mathbf{r}|\mathbf{R}(\mathbf{t}), \boldsymbol{\sigma}) = \frac{1}{2\pi|\mathbf{r}'|^2}(2\hat{\mathbf{r}}'\hat{\mathbf{r}}' - \mathbf{I}) \cdot \boldsymbol{\sigma}, \tag{1.3}$$

where $\mathbf{r}' = \mathbf{r} - \mathbf{R}(\mathbf{t})$ and $\hat{\mathbf{r}}' = \mathbf{r}'/|\mathbf{r}'|$. As expected, the dipolar solution $\mathbf{u}^d$ brings a $1/r^2$ contribution, which is dominant compared to the potential quadrupole term in $1/r^3$ resulting from the confined Stokes doublet. Note that the flow generated by confined self-propelled particles has surprisingly the same angular dependence as the one resulting from confined but passively driven particles (force monopoles).

To summarize, confinement between rigid surfaces *suppresses the force dipole contribution* (from $1/r^2$ to $1/r^3$), *while amplifying the source dipole one* (from $1/r^3$ to $1/r^2$), radically changing the nature of the far-field interactions. In particular, *the distinction between pushers and pullers becomes irrelevant* and the angular symmetry of the singularity dominant under confinement (Fig. 1.2b) strongly contrasts with the one governing interactions in unbounded geometries (Fig. 1.2a). Note that the $1/r^2$ spatial decay remains unchanged, unlike the dimensionality of the system. Confined suspensions are therefore *a borderline case between strong and weak interacting systems* for which large-scale correlated motions typical of strong interacting 3D suspensions might disappear.

1.3 Individual motion of confined anisotropic polar swimmers

Now that we derived the interactions between self-propelled particles in rigidly confined geometries, we shall examine their response to these flows. The objective of this section is to set the equations of motion of a single swimmer in an arbitrary flow field.

We focus our attention to anisotropic swimmers, for which an orientation can be defined. In addition to being anisotropic, most biological swimmers are polar, that is, they have no front-back symmetry. We shall therefore develop a general model that accounts for this interesting characteristic. Let us consider a single anisotropic polar swimmer with center of mass position $\mathbf{R}(t)$ and orientation $\mathbf{p}(t)$ ($|\mathbf{p}|^2 = 1$), swimming with velocity v_s along $\mathbf{p}$. When confined in an arbitrary flow $\mathbf{u}$, the equations governing its motion have been very recently proposed by Brotto *et al.* [20]:

$$\dot{\mathbf{R}} = v_s\,\mathbf{p} + \mu_\perp\,(\mathbf{I} - \mathbf{pp})\cdot\mathbf{u} + \mu_\parallel\,\mathbf{pp}\cdot\mathbf{u} \tag{1.4a}$$

$$\dot{\mathbf{p}} = \nu\,(\mathbf{I} - \mathbf{pp})\cdot\mathbf{u} + \nu'\,(\mathbf{I} - \mathbf{pp})\cdot\nabla\mathbf{u}\cdot\mathbf{p} \tag{1.4b}$$

where $\mu_\parallel$ (resp. $\mu_\perp$) denotes the longitudinal (resp. transverse) mobility coefficient and ν (resp. ν') the polar (resp. anisotropic) rotational mobility coefficient. Reorientation of anisotropic particles due to the flow gradient at a rate $0 < \nu' < 1$ corresponds to the well-known Jeffery's equation, where $\nu' = (A^2-1)/(A^2+1) < 1$ for an ellipsoid particle of aspect ratio A [4]. However, Brotto *et al.* recently showed that in stark contrast to unconfined geometries, rigidly confined anisotopic swimmers undergoing lubricated friction with rigid walls are subject to anisotropic mobility ($\mu_\perp \neq \mu_\parallel$ and $\mu_\perp, \mu_\parallel \neq 1$) and polar ones can in addition reorient because of the flow itself ($\nu \neq 0$) [20]. To gain insight into this new dynamics and the effects of confinement, they derived analytical expressions for these coefficients using the following microscopic dumbbell model.

As sketched in Fig. 1.3, we consider a particle composed of two disks of radius b_1 (resp. b_2) located at $\mathbf{R}_1$ (resp. $\mathbf{R}_2$) connected by a frictionless rigid rod of length $a \gg b_1, b_2$. Because of lubrication, each

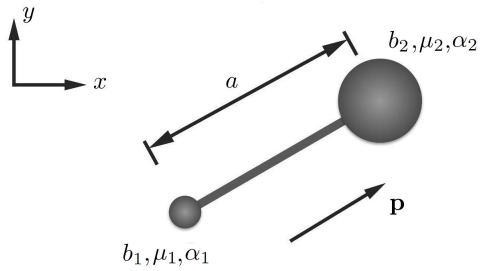

FIG. 1.3: Microscopic dumbbell as a simple model of anisotropic polar swimmer

disk is transported at a velocity $\dot{\mathbf{R}}_i = \mu_i \mathbf{u}(\mathbf{R}_i)$ with a mobility coefficient $0 < \mu_i < 1$ depending on b_i. Moreover, both disks have a different drag coefficients, and thus respond differently to an external force: $\dot{\mathbf{R}}_i = \alpha_i \mathbf{F}$ (where α_i^{-1} is the drag coefficient). Using this notation, we define the center of drag of the swimmer as $\mathbf{R} = (\alpha_2 \mathbf{R}_1 + \alpha_1 \mathbf{R}_2)/(\alpha_1 + \alpha_2)$. The motion of each disk i becomes a mobility problem and results from the superposition of:

- independent self-propulsion at a velocity $v_s \mathbf{p}$,
- passive advection by the external flow (due to other particles) $\mathbf{u}^0(\mathbf{R}_i) \approx \mathbf{u}^0(\mathbf{R}) + (\mathbf{R}_i - \mathbf{R}) \cdot \nabla \mathbf{u}^0(\mathbf{R})$ using a first-order Taylor expansion around the center of drag (with $\mathbf{R}_2 - \mathbf{R}_1 = a\mathbf{p}$),
- advection by the dipolar flow generated by the other disk $\mathbf{u}^d(\mathbf{R}_i | \mathbf{R}_j, \boldsymbol{\sigma}_j)$, with $\boldsymbol{\sigma}_j \approx 2\pi b_j^2 (v_s \mathbf{p} + \mu_j \mathbf{u}^0(\mathbf{R}_j) - \mathbf{u}^0(\mathbf{R}_j))$,
- drag by the rod tension $\mathbf{T}$ which enforces the inextensibility condition $\mathbf{p} \cdot (\dot{\mathbf{R}}_2 - \dot{\mathbf{R}}_1) = 0$.

We derived $\dot{\mathbf{R}}, \dot{\mathbf{p}}$ following these steps (which can be regarded as an elementary method of reflection) and obtained for $\mu_\perp, \mu_\parallel, \nu, \nu'$ slightly different expressions than Brotto *et al.*:

$$\mu_\perp = \frac{1}{\alpha_1 + \alpha_2} \left[\alpha_1 \mu_2 \Big(1 + (1 - \mu_1) \frac{b_1^2}{a^2} \Big) + \alpha_2 \mu_1 \Big(1 + (1 - \mu_2) \frac{b_2^2}{a^2} \Big) \right], \tag{1.5a}$$

$$\mu_\parallel = \frac{1}{\alpha_1 + \alpha_2} \left[\alpha_1 \mu_2 \Big(1 - (1 - \mu_1) \frac{b_1^2}{a^2} \Big) + \alpha_2 \mu_1 \Big(1 - (1 - \mu_2) \frac{b_2^2}{a^2} \Big) \right], \tag{1.5b}$$

$$\nu = \frac{1}{a} \left[\mu_2 \Big(1 + (1 - \mu_1) \frac{b_1^2}{a^2} \Big) - \mu_1 \Big(1 + (1 - \mu_2) \frac{b_2^2}{a^2} \Big) \right], \tag{1.5c}$$

$$\nu' = \frac{1}{\alpha_1 + \alpha_2} (\alpha_1 \mu_1 + \alpha_2 \mu_2), \tag{1.5d}$$

but arrived to the exact same conclusions:

- $\mu_\perp$, $\mu_\parallel$, ν' depend only on the anisotropy (they remain equal after a tail-head permutation) whereas ν is solely due to polarity,
- $0 < \mu_\parallel < \mu_\perp < 1$: the transverse mobility is always greater than the longitudinal one,
- since the μ_i are decreasing functions of b_i, $\nu > 0$ refers to *large-tail* swimmers (for which $b_2 > b_1$) whereas $\nu < 0$ refers to *large-head* swimmers ($b_1 > b_2$).

Considering Eqs. (1.5a), (1.5b) it is natural to define the following coefficients, which will prove to be more relevant in the following:

$$\bar{\mu} = \frac{\mu_\perp + \mu_\parallel}{2} \qquad \tilde{\mu} = \mu_\perp - \mu_\parallel, \tag{1.6}$$

where $0 < \bar{\mu} < 1$ is the average mobility and $0 < \tilde{\mu} < 1$ quantifies the anisotropy of the swimmer.

These derivations prove that symmetry-breaking and momentum absorption due to confinement not only dramatically influences the nature of interactions, but also the response of particles to them. We shall see that the new orientational dynamics characterized by ν leads to fascinating phenomena in which the difference between large-head and large-tail swimmers will become central.

1.4 Continuum description and kinetic model

In this section, we briefly introduce the kinetic model first proposed by Saintillan and Shelley [3, 4] to investigate collective dynamics in active suspensions.

The configuration of particles is described by a continuous distribution function $\Psi(\mathbf{x}, \mathbf{p}, t)$, representing the probability of finding a particle located at position $\mathbf{x}$ with orientation $\mathbf{p}$ at time t (see Fig. 1.4a). The first three moments of Ψ on the unit circle are a very convenient way to describe the general phase properties of the suspension:

- $c(\mathbf{x}, t) = \int \Psi(\mathbf{x}, \mathbf{p}, t)\, \mathrm{d}\mathbf{p}$ yields the local concentration or number of particles per unit area.
- $\mathbf{P}(\mathbf{x}, t) = \frac{1}{c(\mathbf{x},t)} \int \mathbf{p}\Psi(\mathbf{x}, \mathbf{p}, t)\, \mathrm{d}\mathbf{p}$ is the local polarization and describes the mean direction of alignment of particles. Note that $\mathbf{P} = 0$ for an isotropic distribution $\partial\Psi/\partial\mathbf{p} = 0$.
- $\mathbf{Q}(\mathbf{x}, t) = \frac{1}{c(\mathbf{x},t)} \int (\mathbf{pp} - \frac{1}{2}\mathbf{I})\Psi(\mathbf{x}, \mathbf{p}, t)\, \mathrm{d}\mathbf{p}$ represents the local nematic orientation tensor. This second-order symmetric tensor is commonly used in condensed matter physics to describe at least two different types of deformation, in particular in liquid crystals. $Q_{xx} = \frac{1}{2c} \int_{-\pi}^{\pi} \Psi \cos 2\theta\, \mathrm{d}\theta$ quantifies *splay* deformations (Fig. 1.4b) whereas $Q_{xy} = \frac{1}{2c} \int_{-\pi}^{\pi} \Psi \sin 2\theta\, \mathrm{d}\theta$ accounts for *bend* nematic alignment (Fig. 1.4c).[2] It is by definition traceless, such that the isotropic state conveniently corresponds to $\mathbf{Q} = 0$. Its positive eigenvalue quantifies the orientational order whereas the associated eigenvector yields the deformation axis.

By conservation of the total number of particles[3] $N = \int c(\mathbf{x}, t)\, \mathrm{d}\mathbf{x}$, Ψ must satisfy the following continuity equation:

$$\frac{\partial \Psi}{\partial t} = -\nabla \cdot (\Psi\, \dot{\mathbf{R}}) - \nabla_{\mathbf{p}} \cdot (\Psi\, \dot{\mathbf{p}}) + D\, \nabla^2 \Psi + D_R\, \nabla_{\mathbf{p}}^2 \Psi, \tag{1.7}$$

often referred to as Smoluchowski (or advection-diffusion) equation. Here D (resp. D_R) is the translational (resp. rotational) diffusion coefficient and $\nabla_{\mathbf{p}} = (\mathbf{I} - \mathbf{pp})\partial/\partial\mathbf{p}$ the gradient operator on the unit circle.

[2] Integration must be performed over the whole unit circle since Ψ is *not* π-periodic for suspensions of polar swimmers.
[3] Note that this is the only conserved physical quantity.

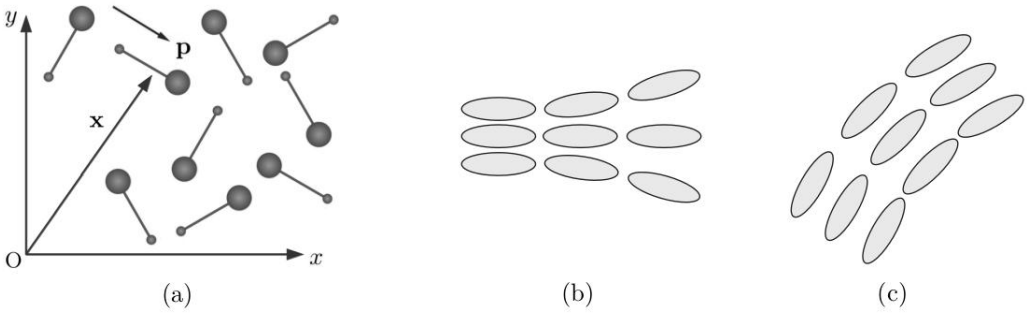

FIG. 1.4: (a) Continuum description of particles configurations in terms of a distribution function $\Psi(\mathbf{x}, \mathbf{p}, t)$ of the center of mass $\mathbf{x}$ and orientation $\mathbf{p}$. (b) Splay mode. (c) Bend mode. Panels (b) and (c) adapted from [18].

As we shall later see, the diffusion coefficients play an important role in the stability. Although biological swimmers typically do not experience thermal noise (their size makes them insensitive to Brownian motion), shape imperfection and noise in their individual swimming mechanism are a first source of diffusion [26, 27] and can be well modeled by constant diffusion coefficients D^0, D_R^0 [13]. Note that the coupling between swimming motion and orientational diffusion (which randomizes the swimming direction) yields an additional translational diffusion coefficient [13]. The resulting random walk process may indeed be modeled using Brenner's generalized Taylor dispersion theory [28, 29] and it can be proved that $D = D^0 + v_s^2/2D_R^0$ in 2D [6]. In addition to this individual diffusion, a second (and often dominant) source of diffusion is attributed to hydrodynamic interactions. It has been suggested that the rotational diffusion coefficient is proportional to the volume fraction, at least for fairly dilute systems [5, 6]. In the dilute limit, we will neglect this source of diffusion[4] ($D_R = D_R^0$), and since D^0 and D_R^0 typically have both low values, we have $D^0 \ll v_s^2/2D_R^0$. It is thus safe to work under the assumption that

$$D = \frac{v_s^2}{2D_R}. \tag{1.8}$$

As we can see in Eqs. (1.4a), (1.4b) the translational and rotational fluxes require the velocity flow field generated by the swimmer distribution Ψ. In the Stokes regime, we obtain this field by linear superposition of elementary dipolar solutions given by Eq. (1.3), weighted by Ψ. This yields the following convolution integral:

$$\mathbf{u}(\mathbf{x}, t) = \int \int_{a<|\mathbf{x}'-\mathbf{x}|<L} \Psi(\mathbf{x}', \mathbf{p}, t)\mathbf{u}^d(\mathbf{x}|\mathbf{x}', \boldsymbol{\sigma})\, \mathrm{d}\mathbf{x}'\, \mathrm{d}\mathbf{p}. \tag{1.9}$$

Note that since $\mathbf{u}^d \sim 1/r^2$, the integration over $\mathbf{x}'$ requires special care. We can for instance assume that the system has a size L, and that particles have a length a (cut-off distance) to ensure convergence. The importance of cancelling the interaction of a swimmer with itself (by excluding the domain $|\mathbf{x}' - \mathbf{x}| < a$) has been discussed by Caussin [18].

[4] As we shall later see in numerical simulations, this assumption requires that we set high individual diffusion rates such that this first source of diffusion (which we explicitely control) dominates over the spurious diffusive effects of interactions.

Chapter 2

Linear Stability Analyses

This chapter aims at investigating the stability of three particular stationary solutions of the continuity equation Eq. (1.7) following the methodology introduced by Saintillan and Shelley [4] and Ezhilan and Saintillan [13]. We start by considering the uniform and isotropic base state, which is clearly the most relevant for biological suspensions before studying the effects of a constant external flow. We finally turn to the evolution of a nearly uniform and aligned suspension. Let us mention that since the stability of anisotropic but fore-aft symmetric particles (for which $\nu = 0$) has already been studied in confined geometries [18], our analysis specifically focuses on the genuine effects of the polar shape of particles.

2.1 Nearly uniform and isotropic suspension

2.1.1 Linearization of the continuity equation

The nearly homogeneous and isotropic state is described by the following perturbed functions:

$$\Psi(\mathbf{x},\mathbf{p},t) = \frac{c_0}{2\pi} + \varepsilon\,\Psi'(\mathbf{x},\mathbf{p},t), \quad \text{and} \quad \mathbf{u}(\mathbf{x},t) = \varepsilon\,\mathbf{u}'(\mathbf{x},t) \tag{2.1}$$

where $|\varepsilon| \ll 1$ such that $\Psi', \mathbf{u}' = \mathcal{O}(1)$. Substituting Eq. (2.1) into Eq. (1.7) and using the change of variables $\mathbf{p} = (\cos\theta, \sin\theta)$ for the angular diffusion term yields, in index notation

$$\begin{aligned}\frac{\partial}{\partial t}\Big(\frac{c_0}{2\pi} + \varepsilon\Psi'\Big) = &-\frac{\partial}{\partial x_i}\left[\Big(\frac{c_0}{2\pi} + \varepsilon\Psi'\Big)\Big(v_s p_i + \mu_{\parallel} p_i p_j \varepsilon u'_j + \mu_{\perp}(\delta_{ij} - p_i p_j)\varepsilon u'_j\Big)\right] \\ &- (\delta_{ij} - p_i p_j)\frac{\partial}{\partial p_j}\left[\Big(\frac{c_0}{2\pi} + \varepsilon\Psi'\Big)\Big(\nu(\delta_{ik} - p_i p_k)\varepsilon u'_k + \nu'(\delta_{ik} - p_i p_k)\varepsilon\frac{\partial u'_k}{\partial x_l}p_l\Big)\right] \\ &+ D\varepsilon\frac{\partial^2\Psi'}{\partial x_i \partial x_i} + D_R\varepsilon\frac{\partial^2\Psi'}{\partial\theta^2}.\end{aligned} \tag{2.2}$$

At order $\mathcal{O}(\varepsilon)$, the first divergence term reduces to

$$\begin{aligned}&-\frac{\partial}{\partial x_i}\left[\varepsilon\Psi' v_s p_i + \varepsilon\frac{c_0}{2\pi}\Big(\mu_{\parallel} p_i p_j u'_j + \mu_{\perp}(\delta_{ij} - p_i p_j)u'_j\Big)\right] \\ &\quad = -\varepsilon\frac{c_0}{2\pi}\Big(\frac{2\pi}{c_0}v_s\frac{\partial\Psi'}{\partial x_i}p_i + \mu_{\parallel} p_i p_j\frac{\partial u'_j}{\partial x_i} + \mu_{\perp}(\delta_{ij} - p_i p_j)\frac{\partial u'_j}{\partial x_i}\Big),\end{aligned} \tag{2.3}$$

and the second yields

$$
\begin{aligned}
&-(\delta_{ij}-p_ip_j)\frac{\partial}{\partial p_j}\left[\varepsilon\frac{c_0}{2\pi}\Big(\nu(\delta_{ik}-p_ip_k)u_k'+\nu'(\delta_{ik}-p_ip_k)\frac{\partial u_k'}{\partial x_l}p_l\Big)\right]\\
&\quad=-\varepsilon\frac{c_0}{2\pi}(\delta_{ij}-p_ip_j)\bigg[-\nu(\delta_{ij}p_ku_k'+\delta_{jk}p_iu_k')+\nu'\Big(\frac{\partial u_i'}{\partial x_j}-\frac{\partial u_k'}{\partial x_l}(\delta_{ij}p_kp_l+\delta_{jk}p_ip_l+\delta_{jl}p_ip_k)\Big)\bigg]\\
&\quad=-\varepsilon\frac{c_0}{2\pi}\bigg[-\nu(2p_ku_k'+p_ju_j'-p_ku_k'-p_ju_j')+\nu'\Big(\frac{\partial u_i'}{\partial x_i}-2\frac{\partial u_k'}{\partial x_l}p_kp_l-\frac{\partial u_i'}{\partial x_l}p_ip_l\\
&\qquad-\frac{\partial u_k'}{\partial x_i}p_kp_i-\frac{\partial u_i'}{\partial x_j}p_ip_j+\frac{\partial u_k'}{\partial x_l}p_kp_l+\frac{\partial u_j'}{\partial x_l}p_jp_l+\frac{\partial u_k'}{\partial x_j}p_kp_j\Big)\bigg]\\
&\quad=-\varepsilon\frac{c_0}{2\pi}\bigg[-\nu p_iu_i'+\nu'\Big(\frac{\partial u_i'}{\partial x_i}-2\frac{\partial u_i'}{\partial x_j}p_ip_j\Big)\bigg].
\end{aligned}
\tag{2.4}
$$

Putting together Eqs. (2.2)-(2.4) yields the linearized continuity equation, in vector notation

$$
\frac{\partial\Psi'}{\partial t}=-v_s\nabla_{\mathbf{x}}\Psi'\cdot\mathbf{p}+\frac{c_0}{2\pi}\Big(\nu\mathbf{u}'\cdot\mathbf{p}-(\mu_\perp+\nu')\nabla\cdot\mathbf{u}'+(\mu_\perp-\mu_\parallel+2\nu')\nabla\mathbf{u}':\mathbf{pp}\Big)+D\nabla_{\mathbf{x}}^2\Psi'+D_R\frac{\partial^2\Psi'}{\partial\theta^2}. \tag{2.5}
$$

In order to decouple the velocity field $\mathbf{u}'$ and its derivatives from this equation, we first need to express $\nabla\cdot\mathbf{u}'$ in terms of Ψ' or the perturbed moments $c=c_0+\varepsilon c', \mathbf{P}=\varepsilon\mathbf{P}', \mathbf{Q}=\varepsilon\mathbf{Q}'$. By definition, we have

$$
\nabla\cdot\mathbf{u}(\mathbf{x},t)=\varepsilon\nabla\cdot\mathbf{u}'(\mathbf{x},t)=\iint\Psi(\mathbf{x}',\mathbf{p},t)\Big(-\boldsymbol{\sigma}\cdot\nabla\delta(\mathbf{x}-\mathbf{x}')\Big)\,\mathrm{d}\mathbf{x}'\,\mathrm{d}\mathbf{p}, \tag{2.6}
$$

where, recalling Eq. (1.4a)

$$
\boldsymbol{\sigma}(\mathbf{x},\mathbf{p},t)=\sigma\Big(v_s\mathbf{p}+(\mu_\perp-1)\varepsilon\mathbf{u}'(\mathbf{x},t)+(\mu_\parallel-\mu_\perp)\mathbf{pp}\cdot\varepsilon\mathbf{u}'(\mathbf{x},t)\Big) \tag{2.7}
$$

Let us now split Eq. (2.6) in three terms, as suggested by Eq. (2.7). The first yields

$$
\begin{aligned}
-\sigma v_s\iint\Psi(\mathbf{x}',\mathbf{p},t)\mathbf{p}\cdot\nabla\delta(\mathbf{x}-\mathbf{x}')\,\mathrm{d}\mathbf{x}'\,\mathrm{d}\mathbf{p}&=-\sigma v_s\int\nabla_{\mathbf{x}}\cdot\Big(\Psi(\mathbf{x},\mathbf{p},t)\mathbf{p}\Big)\,\mathrm{d}\mathbf{p}\\
&=-\sigma v_s\nabla\cdot\int\Psi(\mathbf{x},\mathbf{p},t)\mathbf{p}\,\mathrm{d}\mathbf{p}\\
&=-\sigma v_s\nabla\cdot\Big((c_0+\varepsilon c')\varepsilon\mathbf{P}'\Big)(\mathbf{x},t)\\
&=-\varepsilon\sigma v_s\nabla\cdot(c_0\mathbf{P}')(\mathbf{x},t)+\mathcal{O}(\varepsilon^2).
\end{aligned}
\tag{2.8a}
$$

Similarly, the second term simplifies to

$$
\begin{aligned}
&-\varepsilon\sigma(\mu_\perp-1)\iint\Psi(\mathbf{x}',\mathbf{p},t)\mathbf{u}'(\mathbf{x}',t)\cdot\nabla\delta(\mathbf{x}-\mathbf{x}')\,\mathrm{d}\mathbf{x}'\,\mathrm{d}\mathbf{p}\\
&\quad=-\varepsilon\sigma(\mu_\perp-1)\int\nabla_{\mathbf{x}}\cdot\Big(\Psi(\mathbf{x},\mathbf{p},t)\mathbf{u}'(\mathbf{x},t)\Big)\,\mathrm{d}\mathbf{p}\\
&\quad=-\varepsilon\sigma(\mu_\perp-1)\nabla\cdot(c_0\mathbf{u}')(\mathbf{x},t)+\mathcal{O}(\varepsilon^2),
\end{aligned}
\tag{2.8b}
$$

and the third

$$
\begin{aligned}
&-\varepsilon\sigma(\mu_\parallel-\mu_\perp)\iint\Psi(\mathbf{x}',\mathbf{p},t)\mathbf{pp}\cdot\mathbf{u}'(\mathbf{x}',t)\cdot\nabla\delta(\mathbf{x}-\mathbf{x}')\,\mathrm{d}\mathbf{x}'\,\mathrm{d}\mathbf{p}\\
&\quad=-\varepsilon\sigma(\mu_\parallel-\mu_\perp)\int\nabla_{\mathbf{x}}\cdot\Big(\Psi(\mathbf{x},\mathbf{p},t)\mathbf{pp}\cdot\mathbf{u}'(\mathbf{x},t)\Big)\,\mathrm{d}\mathbf{p}\\
&\quad=-\varepsilon\sigma(\mu_\parallel-\mu_\perp)\nabla\cdot\Big(\frac{c_0\mathbf{u}'}{2}\Big)(\mathbf{x},t)+\mathcal{O}(\varepsilon^2).
\end{aligned}
\tag{2.8c}
$$

Summing the contributions given by Eqs. (2.8a)-(2.8c), we rewrite Eq. (2.6) as

$$\varepsilon\nabla\cdot\mathbf{u}' = \varepsilon\sigma\nabla\cdot\left[-v_s c_0\mathbf{P}' + \left(1-\frac{\mu_\perp+\mu_\parallel}{2}\right)c_0\mathbf{u}'\right] + \mathcal{O}(\varepsilon^2), \tag{2.9}$$

which, at leading order in ε, simplifies to

$$\nabla\cdot\mathbf{u}' = -fv_s\nabla\cdot\mathbf{P}', \tag{2.10}$$

where we defined

$$f = \frac{\sigma c_0}{1-\sigma c_0(1-\bar{\mu})}. \tag{2.11}$$

Let us give a physical interpretation of f. Since the dipole strength σ is typically twice the particle area (for a disk shape), $\sigma c_0/2$ can be interpreted as a *surface fraction* (percentage of total surface covered by the particles). For this reason, $\sigma c_0 = 2$ is the absolute theoretical limit (it represents square particles packed without fluid in between). We shall however choose a more physical limit corresponding to particles filling half of the suspension: $\sigma c_0 = 1$ (this prevents f from blowing up). Hence, working in the dilute limit means for us $\sigma c_0 \ll 1$. It follows that f can be interpreted as a *corrected double surface fraction* ($f > 2(\sigma c_0/2)$), inceasing with lower average mobility $\bar{\mu}$.

2.1.2 Fourier transform of the linearized equation

We can now make analytical progress by assuming that the perturbation variables Ψ' and $\mathbf{u}'$ take the form of plane waves

$$\Psi'(\mathbf{x},\mathbf{p},t) = \tilde{\Psi}(\mathbf{k},\mathbf{p})\exp(i\mathbf{k}\cdot\mathbf{x}+\alpha t) \quad \text{and} \quad \mathbf{u}'(\mathbf{x},t) = \tilde{\mathbf{u}}(\mathbf{k})\exp(i\mathbf{k}\cdot\mathbf{x}+\alpha t) \tag{2.12}$$

where $\mathbf{k} = k\hat{\mathbf{k}}$ is the wave vector and α the complex growth rate. This spatial Fourier transform will enable us to decouple the velocity and its derivatives from our linear stability equation. Defining $\tilde{\mathbf{P}}(\mathbf{k})$ as the Fourier amplitude of $\mathbf{P}'$, Eq. (2.10) yields, in the Fourier space

$$\widetilde{\nabla\cdot\mathbf{u}'} = -ikfv_s\tilde{\mathbf{P}}\cdot\hat{\mathbf{k}}. \tag{2.13}$$

Recalling the fact that $\mathbf{u}$ is potential, we can use this to deduce the Fourier transform of $\mathbf{u}'$ itself by considering the (potential) pressure $\Pi'(\mathbf{x},t) = \tilde{\Pi}(\mathbf{k})\exp(i\mathbf{k}\cdot\mathbf{x}+\alpha t)$. Combining Eqs. (1.1), (2.13) we indeed get

$$\frac{h^2}{12\eta}k^2\tilde{\Pi} = -ikfv_s\tilde{\mathbf{P}}\cdot\hat{\mathbf{k}}. \tag{2.14}$$

Using this expression for $\tilde{\Pi}$ and Eq. (1.1) again, it follows that

$$\widetilde{\mathbf{u}'} = -i\mathbf{k}\left(-\frac{1}{k^2}ikfv_s\tilde{\mathbf{P}}\cdot\hat{\mathbf{k}}\right) = -fv_s(\tilde{\mathbf{P}}\cdot\hat{\mathbf{k}})\hat{\mathbf{k}}, \tag{2.15}$$

from which it is straightforward to compute the Fourier transform of the velocity gradient

$$\widetilde{\nabla\mathbf{u}} = -ikfv_s(\tilde{\mathbf{P}}\cdot\hat{\mathbf{k}})\hat{\mathbf{k}}\hat{\mathbf{k}}. \tag{2.16}$$

Our objective is now to rewrite the linearized equation Eq. (2.5) in terms of Fourier amplitudes. Combining Eqs. (2.13), (2.15) and (2.16) yields

$$\begin{aligned}\alpha\tilde{\Psi} &= -v_s i\mathbf{k}\tilde{\Psi}\cdot\mathbf{p} + \frac{c_0}{2\pi}\Big(\nu(\tilde{\mathbf{u}}\cdot\mathbf{p}) - (\mu_\perp+\nu')\widetilde{\nabla\cdot\mathbf{u}} + (\mu_\perp-\mu_\parallel+2\nu')\widetilde{\nabla\mathbf{u}}\!:\!\mathbf{pp}\Big) - Dk^2\tilde{\Psi} + D_R\frac{\partial^2\tilde{\Psi}}{\partial\theta^2}\\ &= -iv_s\mathbf{k}\cdot\mathbf{p}\tilde{\Psi} + fv_s\frac{c_0}{2\pi}\Big(-\nu(\tilde{\mathbf{P}}\cdot\hat{\mathbf{k}})\hat{\mathbf{k}}\cdot\mathbf{p} + (\mu_\perp+\nu')ik(\tilde{\mathbf{P}}\cdot\hat{\mathbf{k}})\\ &\quad -(\mu_\perp-\mu_\parallel+2\nu')ik(\tilde{\mathbf{P}}\cdot\hat{\mathbf{k}})\hat{\mathbf{k}}\hat{\mathbf{k}}\!:\!\mathbf{pp}\Big) - k^2D\tilde{\Psi} + D_R\frac{\partial^2\tilde{\Psi}}{\partial\theta^2}.\end{aligned} \tag{2.17}$$

Without loss of generality, we write $\tilde{\Psi}(\mathbf{k},\mathbf{p}) = \tilde{\Psi}(\theta)$ where $\theta = \cos^{-1}(\hat{\mathbf{k}}\cdot\mathbf{p})$ and expand it as a series of Fourier modes $\tilde{\Psi}(\theta) = \sum_{n=-\infty}^{+\infty}\tilde{\Psi}_n\exp(in\theta)$. By orthogonality, the projection of the Fourier transform of the polarization on the unitary wave vector is simply

$$\tilde{\mathbf{P}}\cdot\hat{\mathbf{k}} = \Big(\frac{1}{c_0}\int_0^{2\pi}\mathbf{p}\sum_{n=-\infty}^{+\infty}\tilde{\Psi}_n\exp(in\theta)\,\mathrm{d}\theta\Big)\cdot\hat{\mathbf{k}} = \frac{1}{c_0}\sum_{n=-\infty}^{+\infty}\tilde{\Psi}_n\int_0^{2\pi}\cos\theta\exp(in\theta)\,\mathrm{d}\theta = \frac{\pi}{c_0}(\tilde{\Psi}_{-1}+\tilde{\Psi}_1). \tag{2.18}$$

Eventually, we use Eq. (2.18) to simplify Eq. (2.17), and we find that

$$\begin{aligned}(\alpha+k^2D)\tilde{\Psi} &= -ikv_s\cos\theta\tilde{\Psi} + \frac{fv_s}{2}\Big(-\nu(\tilde{\Psi}_{-1}+\tilde{\Psi}_1)\cos\theta + ik(\mu_\perp+\nu')(\tilde{\Psi}_{-1}+\tilde{\Psi}_1)\\ &\quad -ik(\mu_\perp-\mu_\parallel+2\nu')(\tilde{\Psi}_{-1}+\tilde{\Psi}_1)\cos^2\theta\Big) + D_R\frac{\partial^2\tilde{\Psi}}{\partial\theta^2}.\end{aligned} \tag{2.19}$$

2.1.3 Non-dimensionalization and eigenvalue problem

The stability equation for the Fourier amplitude Eq. (2.19) can be written as an eigenvalue problem for the discrete Fourier modes $\tilde{\Psi}_n$. Dividing by D_R we indeed obtain the following dimensionless expression:

$$\begin{aligned}\frac{\alpha+k^2D}{D_R}\sum_{n=-\infty}^{+\infty}\tilde{\Psi}_n e^{in\theta} &= \sum_{n=-\infty}^{+\infty}\Big(-ik\frac{v_s}{2D_R}(\tilde{\Psi}_{n-1}+\tilde{\Psi}_{n+1}) - n^2\tilde{\Psi}_n\Big)e^{in\theta} + \frac{fv_s}{2D_R}(\tilde{\Psi}_{-1}+\tilde{\Psi}_1)\Big(ik\frac{\mu_\perp+\mu_\parallel}{2}\\ &\quad -\frac{\nu}{2}(e^{i\theta}+e^{-i\theta}) - ik\frac{\mu_\perp-\mu_\parallel+2\nu'}{2}(e^{i2\theta}+e^{-i2\theta})\Big).\end{aligned} \tag{2.20}$$

We notice that the translational diffusion simply shifts the real part of α by $-k^2D$, damping potential instabilities with increasing wavenumber. As D tends to smooth out the concentration field, this observation is consistent with the expectation that its works against the formation of concentration instabilities at finite wavenumbers. Note that Eq. (2.20) features the following interesting lengthscale:

$$l = \frac{v_s}{2D_R}, \tag{2.21}$$

which we interpret as the distance travelled by a swimmer before losing its orientation because of diffusion. To gain insight into the physical phenomena involved in this stability problem, let us further define the following five dimensionless parameters:

$$Pe = f\nu l, \qquad \bar{H} = f\bar{\mu}, \qquad \widetilde{H} = f(\tilde{\mu}+2\nu'), \qquad \alpha' = \frac{\alpha}{D_R}, \qquad k' = kl. \tag{2.22}$$

Using these notations and the relation between D and D_R established in Eq. (1.8), we find that

$$\frac{\alpha + k^2 D}{D_R} = \alpha' + 2k'^2. \tag{2.23}$$

Recall that the sign of ν, and hence, of the *signed Péclet number* Pe is different for large-head ($Pe < 0$) and large-tail ($Pe > 0$) swimmers. Its absolute value quantifies the ratio between rotation induced by self-advection of particles and rotational diffusion (recall $\nu l \sim l/a$ i.e. Pe scales as the ratio between swimming distance with orientation memory l and dumbbell length a). In other words, $|Pe|$ is maximal when (i) swimmers are relatively close to each other (large f), (ii) they travel long distances with memory of their orientation (large l), (iii) their orientation responds sensitively to the flow (large $|\nu|$). We can therefore already speculate that a large absolute value of the Péclet number may trigger large-scale correlated motion. In contrast with Pe which results from the *polarity* (fore-aft asymmetry) of swimmers, $\bar{H}$ quantifies *mobility* while $\widetilde{H}$ is a sole consequence of *anisotropy*. We shall also point out that $0 < \bar{H} < 1$ in the limit $\sigma c_0 < 1$, and as $\widetilde{H}$ may blow up for $\{\sigma c_0 \to 1,\ \bar{\mu} \to 0\}$ we will assume $0 < \widetilde{H} < 2$ in the reasonable limit $\sigma c_0 < 1/2$ (i.e. 25% surface fraction). With these notations, Eq. (2.20) becomes

$$\begin{aligned}(\alpha' + 2k'^2) \sum_{n=-\infty}^{+\infty} \tilde{\Psi}_n e^{in\theta} = \sum_{n=-\infty}^{+\infty} \Big(&- ik'(\tilde{\Psi}_{n-1} + \tilde{\Psi}_{n+1}) - n^2 \tilde{\Psi}_n \Big) e^{in\theta} \\ &+ (\tilde{\Psi}_{-1} + \tilde{\Psi}_1)\Big(ik'\bar{H} - \frac{Pe}{2}(e^{i\theta} + e^{-i\theta}) - ik'\frac{\widetilde{H}}{2}(e^{i2\theta} + e^{-i2\theta}) \Big),\end{aligned} \tag{2.24}$$

or equivalently, in matrix form

$$(\alpha' + 2k'^2) \begin{pmatrix} \vdots \\ \tilde{\Psi}_{-3} \\ \tilde{\Psi}_{-2} \\ \tilde{\Psi}_{-1} \\ \tilde{\Psi}_0 \\ \tilde{\Psi}_1 \\ \tilde{\Psi}_2 \\ \tilde{\Psi}_3 \\ \vdots \end{pmatrix} = \begin{pmatrix} \ddots & \ddots & & & & & & & & \\ \ddots & -9 & -ik' & & & & & & & \\ & -ik' & -4 & -ik'(1+\frac{\widetilde{H}}{2}) & & -ik'\frac{\widetilde{H}}{2} & & & & \\ & & -ik' & -(1+\frac{Pe}{2}) & -ik' & -\frac{Pe}{2} & & & & \\ & & & -ik'(1-\bar{H}) & 0 & -ik'(1-\bar{H}) & & & & \\ & & & -\frac{Pe}{2} & -ik' & -(1+\frac{Pe}{2}) & -ik' & & & \\ & & & -ik'\frac{\widetilde{H}}{2} & & -ik'(1+\frac{\widetilde{H}}{2}) & -4 & -ik' & & \\ & & & & & & -ik' & -9 & \ddots & \\ & & & & & & & \ddots & \ddots & \end{pmatrix} \cdot \begin{pmatrix} \vdots \\ \tilde{\Psi}_{-3} \\ \tilde{\Psi}_{-2} \\ \tilde{\Psi}_{-1} \\ \tilde{\Psi}_0 \\ \tilde{\Psi}_1 \\ \tilde{\Psi}_2 \\ \tilde{\Psi}_3 \\ \vdots \end{pmatrix} \tag{2.25}$$

The focus of the following section is to solve this eigenvalue problem for different values of $Pe, \bar{H}, \widetilde{H}, k'$ and determine whether or not it admits positive values for the real part of α', meaning instability of the homogeneous and isotropic base state. Taking into account a relatively small number of modes (say $2N+1$ modes), we should converge quickly since we focus our attention on the single eigenvalue with the largest real part. For such a solution of interest α'^m, the corresponding mode $\tilde{\Psi}^m(\theta)$ is computed in the real space using its $2N+1$ components $\tilde{\Psi}^m_n \in \mathbb{C}$: $\tilde{\Psi}^m(\theta) = Re\Big(\sum_{n=-N}^{N} \tilde{\Psi}^m_n \exp(in\theta) \Big)$. Alternatively, considering the special pattern of the matrix, this reduces to

$$\tilde{\Psi}^m(\theta) = Re(\tilde{\Psi}^m_0) + 2\sum_{n=1}^{N} Re(\tilde{\Psi}^m_n)\cos n\theta. \tag{2.26}$$

Note that $Re(\tilde{\Psi}_0^m) \neq 0$ corresponds to a mode involving concentration fluctuations. Similarly, a large first order harmonic $2Re(\tilde{\Psi}_1^m)$ indicates a polarization mode and the second harmonic $2Re(\tilde{\Psi}_2^m)$ a splay mode, in consistency with the notions introduced in Sec. 1.4.

2.1.4 Large-scale instability of large-head swimmers

Solving the eigenvalue problem Eq. (2.25) numerically showed that suspensions of large-head swimmers for which $Pe < -1$ are always unstable at low wavenumbers.

Fig. 2.1a shows the two greatest real eigenvalues $Re(\alpha')$ as a function of k' for different values of Pe, and their corresponding imaginary part. We notice that time oscillations start at a finite k'^* when the

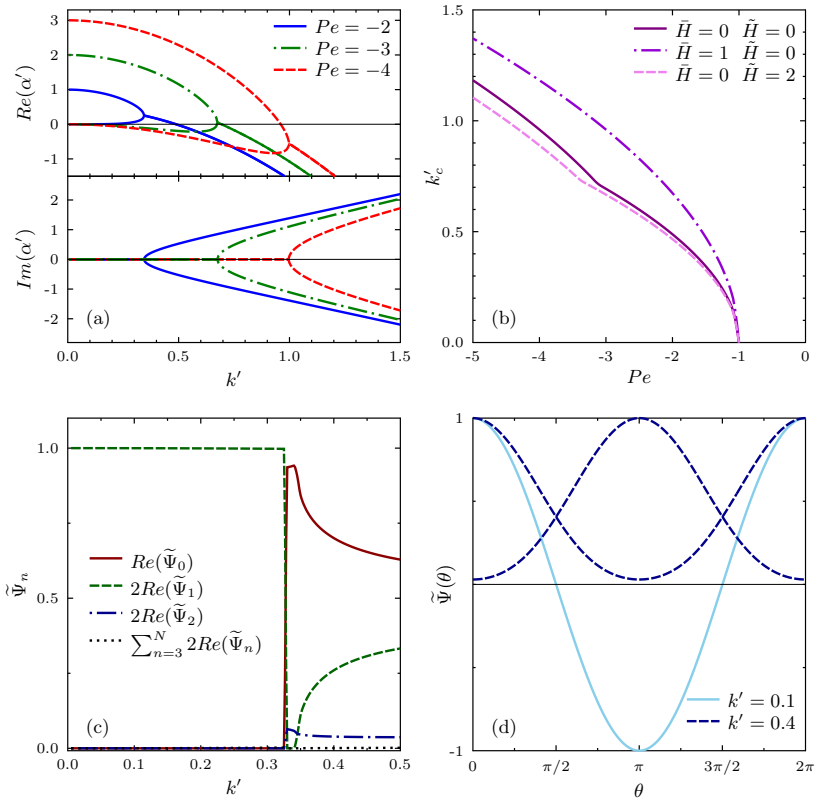

FIG. 2.1: Numerical solutions of the stability eigenvalue problem for $\bar{H} = \widetilde{H} = 0$. (a) Real and imaginary growth rate for various unstable Péclet numbers. (b) Critical wavenumber k'_c as a function of Pe for extreme values of $\bar{H}, \widetilde{H}$, showing the little influence of these parameters. (c) Unstable Fourier modes $\tilde{\Psi}_n$: reparitition of the zeroth, first, second and higher-orders harmonics as a function of k' for $Pe = -2$. (d) Shape of unstable mode $\tilde{\Psi}(\theta)$ for $Pe = -2$ in the two distinct regimes identified on (a) and (c).

two real eigenvalues become equal and form a single branch, which can happen in the unstable regime provided that $Pe > -3$. In the long wavelength limit $k' = 0$ we found $Re(\alpha') = -(1 + Pe)$, confirming previous results by Brotto *et al.* [20]. Instability therefore always occurs when $Pe < -1$ at sufficiently low wavenumbers and lower values of Pe (i.e. larger $|Pe|$) increase the critical wavenumber k'_c, defined

as the k' value for which $Re(\alpha') = 0$), as shown in Fig. 2.1b. This figure also proves that this behavior is surprisingly independent of the mobility and anisotropy dimensionless parameters $\bar{H}, \widetilde{H}$. A way to interpret this point of stability transition is to consider the smallest unstable wavelength L_c

$$\frac{L_c}{l} = \frac{2\pi}{k'_c}, \tag{2.27}$$

where L_c is non-dimensionalized by the distance l over which the orientation of a swimmer can overcome diffusion. This means that systems containing perturbations of wavelength $L > L_c$ are unstable, and as α' is a decreasing function of k', we expect the largest instability to always dominate. Considering a periodic box, L_c may be thought of as the *critical system size*, above which it becomes unstable.

As shown in Fig. 2.1c and Fig. 2.1d, this instability involves pure longitudinal polarization for $k' < k'^*$, and a strong coupling between concentration, polarization and (to a lesser extent) splay for $k' > k'^*$. For $Pe < -3$ or in very large systems ($L/l > 2\pi/k'^*$), we therefore expect large-scale spatial fluctuations of particles aligning along and against the directions of large-wavelength perturbations. In addition to those (static) polarization fluctuations, $Pe < -3$ allows medium-sized systems ($2\pi/k'_c < L/l < 2\pi/k'^*$) to exhibit concentration and splay fluctuations. We further predict in that case that these waves propagate with time with higher phase speed for smaller systems (see Fig. 2.1a).

As it clearly emerges from this analysis, anisotropy alone does not lead to instability in the dilute limit, as Caussin concluded in a previous analysis with $\nu = 0$ [18]. The underlying mechanism of the instability presented here may only be physically understood considering the *dipolar symmetry* of the interactions and the *polar shape* of particles. Eq. (2.10) indeed shows that a local polarization perturbation $\delta\mathbf{P}$ result in a fluid flow in the opposite direction $\delta\mathbf{u} = -fv_s\delta\mathbf{P}$. Since large-heads align against the flow $\delta\mathbf{u}$ (i.e. along $\delta\mathbf{P}$), they might end up increasing the perturbation if their rate of reorientation $|\nu|$ is great enough to overcome rotational diffusion ($|Pe|$ precisely quantifies this ratio) [20]. The existence of two different modes according to the system size is however still not well understood.

2.2 Influence of a uniform external flow

In this section, we shall see how the previous stability results are modified when the suspension is subject to a constant and uniform external flow $\mathbf{U}_0$. In consistency with the results of the previous analysis, we focus here on the effect of polarity ν and assume that $\mu_\perp = \mu_\parallel = 1$, $\nu' = 0$, significantly simplifying the following derivations. Our expectation is that the prescribed flow will stabilize the suspension by controlling the orientations of swimmers, as found in a similar analysis carried out in the 3D case for a simple shear flow (recall that unconfined particles can only reorient with flow gradients) [7].

2.2.1 Polar steady state

We first seek a spatially uniform steady solution of the equations of the form $c_0\Psi_0(\mathbf{p})$, which will serve as base state for our stability analysis. Under these assumptions, we can rewrite the continuity equation

Eq. (1.7) and the angular flux Eq. (1.4b) as

$$-\nabla_{\mathbf{p}} \cdot (\Psi_0 \, \dot{\mathbf{p}}) = 0 \qquad \text{with} \qquad \dot{\mathbf{p}} = \nu \, (\mathbf{I} - \mathbf{pp}) \cdot \mathbf{U}_0 - D_R \nabla_{\mathbf{p}} \ln \Psi_0. \tag{2.28}$$

The solution we seek is obtained by setting the angular flux velocity $\dot{\mathbf{p}}$ to zero

$$\nabla_{\mathbf{p}} \ln \Psi_0 = \frac{\nu}{D_R} \, (\mathbf{I} - \mathbf{pp}) \cdot \mathbf{U}_0. \tag{2.29}$$

Eq. (2.29) simply expresses the balance between rotational diffusion and alignment of the particles along the external flow. It is straightforward to show that the corresponding base state is

$$\Psi_0(\mathbf{p}) = A \exp\left(\frac{\nu}{D_R} \mathbf{U}_0 \cdot \mathbf{p}\right), \tag{2.30}$$

where the integration constant A is determined to normalize Ψ_0 according to $\int \Psi_0(\mathbf{p}) \, \mathrm{d}\mathbf{p} = 1$. Without loss of generality, we set $\mathbf{U}_0 = U_0 \mathbf{e}_x$ and $\theta = \cos^{-1}(\mathbf{p} \cdot \mathbf{e}_x)$, and rewrite this polar state as

$$\Psi_0(\theta) = A \exp(\xi \cos\theta), \quad \text{with} \quad \xi = \frac{\nu U_0}{D_R}, \tag{2.31}$$

where ξ measures the nondimensional flow strength (this uncovers a new velocity scale D_R/ν in the system). Fig. 2.2a illustrates the base states corresponding to various ξ. We shall also introduce the polarization $\mathbf{P}_0 = P_0 \mathbf{e}_x$, which will prove useful in the following. By definition we have

$$P_0 = \int \Psi_0(\mathbf{p}) \mathbf{p} \cdot \mathbf{e}_x \, \mathrm{d}\mathbf{p} = \frac{\int_0^{2\pi} \exp(\xi \cos\theta) \cos\theta \, \mathrm{d}\theta}{\int_0^{2\pi} \exp(\xi \cos\theta) \, \mathrm{d}\theta}. \tag{2.32}$$

As shown on Fig. 2.2b, $P = 0$ obviously corresponds to the isotropic state $\xi = 0$ considered in the previous section, while complete polarization $P = 1$ could only be attained in the limit $\xi \to \infty$.

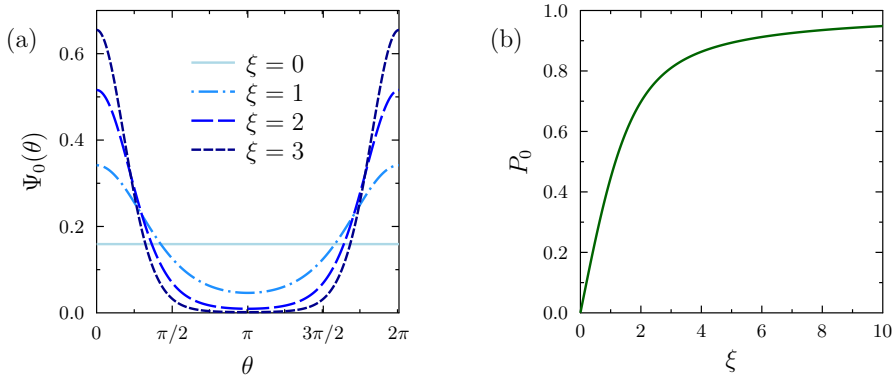

FIG. 2.2: Polar base state of an uniform suspension with constant imposed flow. (a) Normalized orientation distribution $\Psi_0(\theta)$ (θ is the angle with the flow) for various nondimensional flow strengths ξ. (b) Base state polarization P_0 as a function of ξ.

2.2.2 Linearized equation and eigenvalue problem

Let us now consider a small perturbation Ψ' of the distribution function with respect to Ψ_0:

$$\Psi(\mathbf{x}, \mathbf{p}, t) = c_0 \Psi_0(\mathbf{p}) + \varepsilon \Psi'(\mathbf{x}, \mathbf{p}, t), \tag{2.33}$$

where again $|\varepsilon| \ll 1$, $\Psi' = \mathcal{O}(1)$ and similar perturbations are assumed for the other variables. Linearizing Eq. (1.7) in a similar way as in the isotropic case, we derived the following equation for the evolution of the perturbation:

$$\begin{aligned}\frac{\partial \Psi'}{\partial t} = &-\nabla\Psi' \cdot (v_s \mathbf{p} + \mathbf{U}_0) - c_0 \Psi_0 \nabla \cdot \mathbf{u}' - \nu\Big(\nabla_p \Psi'(\mathbf{I} - \mathbf{pp}) \cdot \mathbf{U}_0 \\ &+ c_0 \nabla_p \Psi_0 (\mathbf{I} - \mathbf{pp}) \cdot \mathbf{u}' - \Psi' \mathbf{U}_0 \cdot \mathbf{p} - c_0 \Psi_0 \mathbf{u}' \cdot \mathbf{p}\Big) + D\nabla^2 \Psi' + D_R \nabla_p^2 \Psi'.\end{aligned} \tag{2.34}$$

To decouple the velocity field from this equation, we can show that

$$\nabla \cdot \mathbf{u}' = -f v_s \Big(\nabla c' \cdot \mathbf{P}_0 + \nabla \cdot \mathbf{P}'\Big), \tag{2.35}$$

where $f = \sigma c_0$, $\mathbf{P}_0 = P_0 \mathbf{e}_x$. We can check that if $U_0 = P_0 = 0$, Eqs. (2.34), (2.35) indeed reduce to Eqs. (2.5), (2.10) obtained in the isotropic case.

We now proceed to study these perturbations in the Fourier space, and write $\Psi'(\mathbf{x}, \mathbf{p}, t) = \tilde{\Psi} \exp(i\mathbf{k} \cdot \mathbf{x} + \alpha t)$, $\mathbf{u}'(\mathbf{x}, t) = \tilde{\mathbf{u}} \exp(i\mathbf{k} \cdot \mathbf{x} + \alpha t)$, with $\mathbf{k} = k\hat{\mathbf{k}}$ the plane wave vector and α the complex growth rate. Standard manipulations described previously yield for the velocity field

$$\widetilde{\nabla \cdot \mathbf{u}'} = -ikfv_s\Big(P_0 \tilde{c}\, \hat{\mathbf{k}} \cdot \mathbf{e}_x + \tilde{\mathbf{P}} \cdot \hat{\mathbf{k}}\Big), \tag{2.36a}$$

$$\widetilde{\mathbf{u}'} = -fv_s\Big(P_0 \tilde{c}\, (\hat{\mathbf{k}} \cdot \mathbf{e}_x)\hat{\mathbf{k}} + (\tilde{\mathbf{P}} \cdot \hat{\mathbf{k}})\hat{\mathbf{k}}\Big). \tag{2.36b}$$

As we can see, an important difference with the isotropic case is the dependence of the results on the direction $\hat{\mathbf{k}}$ of the wave with respect to the base state alignment direction $\mathbf{e}_x$. It is therefore necessary to introduce the second angle $\Theta = \cos^{-1}(\hat{\mathbf{k}} \cdot \mathbf{e}_x)$. Using these notations, the Fourier transform of the linearized equation Eq. (2.34) is

$$\begin{aligned}(\alpha + k^2 D)\tilde{\Psi} = \tilde{\Psi}\Big(&- ik(v_s \cos(\theta - \Theta) + U_0 \cos\Theta) + \nu U_0 \cos\theta\Big) + \nu U_0 \frac{\partial \tilde{\Psi}}{\partial \theta} \sin\theta + c_0 \Psi_0 \Big(P_0 \tilde{c} \cos\Theta \\ &+ \tilde{\mathbf{P}} \cdot \hat{\mathbf{k}}\Big)\Big(f v_s ik + f v_s \nu \xi(\cos\Theta - \cos(\theta - \Theta) - f v_s \nu \cos(\theta - \Theta)\Big) + D_R \frac{\partial^2 \tilde{\Psi}}{\partial \theta^2}.\end{aligned} \tag{2.37}$$

This eigenvalue problem may be written $(\alpha + k^2 D)\tilde{\Psi} = \mathcal{L}[\tilde{\Psi}]$, and by expanding $\tilde{\Psi}$ in Fourier modes θ: $\tilde{\Psi}(\theta) = \sum_{n=-\infty}^{+\infty} \tilde{\Psi}_n \exp(in\theta)$, we formally get $(\alpha + k^2 D) \sum_{n=-\infty}^{+\infty} \tilde{\Psi}_n \exp(in\theta) = \sum_{n=-\infty}^{+\infty} \mathcal{L}[\exp(in\theta)]\tilde{\Psi}_n$. Non-dimensionalizing by D_R indeed yields

$$\begin{aligned}(\alpha' + 2k'^2) \sum_{n=-\infty}^{+\infty} \tilde{\Psi}_n \exp(in\theta) = &\Big[- 2ik'\Big(\cos(\theta - \Theta) + \frac{U_0}{v_s} \cos\Theta\Big) + \xi \cos\theta\Big] \sum_{n=-\infty}^{+\infty} \tilde{\Psi}_n \exp(in\theta) \\ &+ \xi \sum_{n=-\infty}^{+\infty} in \tilde{\Psi}_n \exp(in\theta) \sin\theta + \pi \Psi_0(\theta) \Bigg[\Big[\tilde{\Psi}_{-1} \exp(-i\Theta) \\ &+ \tilde{\Psi}_1 \exp(i\Theta) + 2P_0 \tilde{\Psi}_0 \cos\Theta\Big]\Big[2fik' + 2Pe\Big(\xi(\cos\Theta - \cos(\theta - \Theta)) \\ &- \cos(\theta - \Theta)\Big)\Big]\Bigg] - \sum_{n=-\infty}^{+\infty} n^2 \tilde{\Psi}_n \exp(in\theta),\end{aligned} \tag{2.38}$$

where the nondimensional parameters α', k' and Pe are defined in Eq. (2.22). Applying the linear operator $(1/2\pi)\int_0^{2\pi}\exp(-im\theta)\,\mathrm{d}\theta$ to Eq. (2.38), we write this eigenvalue problem in matrix form. Formally,

$$(\alpha' + 2k'^2)\tilde{\Psi}_m = \sum_{n=-\infty}^{+\infty} \underbrace{\frac{1}{2\pi}\int_0^{2\pi} \mathcal{L}[\exp(in\theta)]\exp(-im\theta)\,\mathrm{d}\theta}_{A_{mn}} \tilde{\Psi}_n. \tag{2.39}$$

Applying this procedure to Eq. (2.38) yields for the coefficients A_{mn}

$$A = \begin{pmatrix}
\ddots & \ddots & & \vdots & \vdots & \vdots & & & \\
\ddots & B_1 & B_2 & \exp(-i\Theta)B_4 & (2P_0\cos\Theta)B_4 & \exp(i\Theta)B_4 & & & \\
 & B_3 & B_1 & B_2+\exp(-i\Theta)B_4 & (2P_0\cos\Theta)B_4 & \exp(i\Theta)B_4 & & & \\
 & & B_3 & B_1+\exp(-i\Theta)B_4 & B_2+(2P_0\cos\Theta)B_4 & \exp(i\Theta)B_4 & & & \\
 & & & B_3+\exp(-i\Theta)B_4 & B_1+(2P_0\cos\Theta)B_4 & B_2+\exp(i\Theta)B_4 & & & \\
 & & & \exp(-i\Theta)B_4 & B_3+(2P_0\cos\Theta)B_4 & B_1+\exp(i\Theta)B_4 & B_2 & & \\
 & & & \exp(-i\Theta)B_4 & (2P_0\cos\Theta)B_4 & B_3+\exp(i\Theta)B_4 & B_1 & B_2 & \\
 & & & \exp(-i\Theta)B_4 & (2P_0\cos\Theta)B_4 & \exp(i\Theta)B_4 & B_3 & B_1 & \ddots \\
 & & & \vdots & \vdots & \vdots & & \ddots & \ddots
\end{pmatrix} \tag{2.40}$$

where the diagonal, superdiagonal and subdiagonal coupling terms are respectively

$$B_1 = -2ik'\frac{U_0}{v_s}\cos\Theta - m^2, \tag{2.41a}$$

$$B_2 = -ik'\exp(i\Theta) - \xi\frac{m}{2}, \tag{2.41b}$$

$$B_3 = -ik'\exp(-i\Theta) + \xi\frac{m}{2}, \tag{2.41c}$$

and m denotes the row number. Finally, the integral terms B_4 on the vertical bands, responsible for the coupling of all modes with the concentration and polarization ones, must be computed numerically:

$$B_4 = \int_0^{2\pi}\left[Pe\Big(\xi\Big(\cos\Theta - \cos(\theta-\Theta)\Big) - \cos(\theta-\Theta)\Big) + ik'f\right]\Psi_0(\theta)\exp(-im\theta)\,\mathrm{d}\theta. \tag{2.41d}$$

We notice that the main parameters of interest in this eigenvalue problem are ξ and Θ, and that the ratio U_0/v_s only plays a (limited) role at finite wavenumbers $k' > 0$, which we neglect in the following.

2.2.3 Stabilization of large-heads

After solving this eigenvalue problems numerically, we demonstrate that the flow has a stabilizing effect on large-head suspensions, which we recall are known to be unstable for $Pe < -1$ in the isotropic case $\xi = 0$ at $k' = 0$. As shown on Fig. 2.3a, the unstable critical Péclet number in the long-wavelength limit ($k' = 0$) is severely decreased as the nondimensional flow strength ξ increases (here $\Theta = 0$). Investigation of the Θ-dependence (see Fig. 2.3b) further shows that $\Theta = 0$ or $\Theta = \pi$ are the most effective angles[1], at least for $|\xi| \gtrsim 1$, but $\Theta = \pi/2$ is surprisingly found to be equivalent for $|\xi| \lesssim 1$. Eventually, Fig. 2.3c analyzes

[1]Note the equivalence of $\Theta = 0$ and $\Theta = \pi$ (and hence of ξ and $-\xi$) in this problem, explaining why we keep taking $\xi > 0$ values as examples, even though large-heads are strictly speaking characterized by $\xi < 0$.

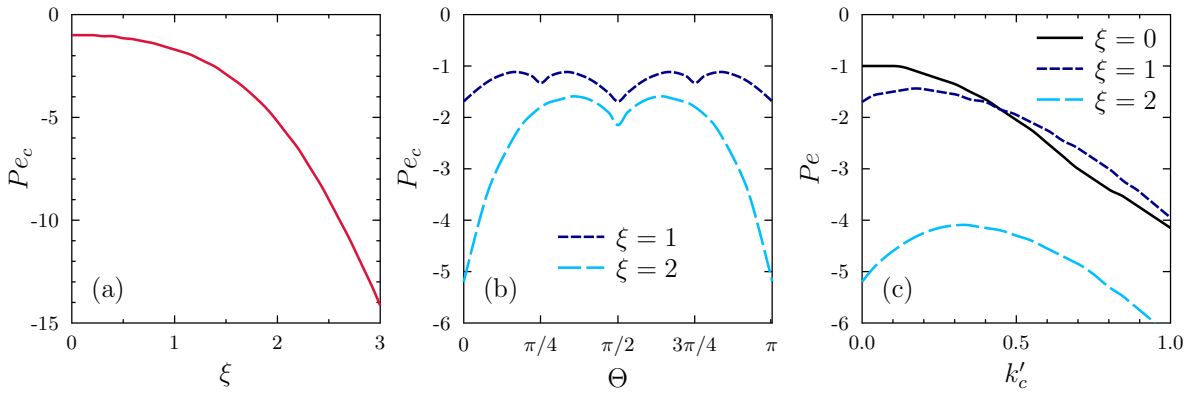

FIG. 2.3: Added stability with an external flow in large-heads suspensions ($f = 0$, $U_0/v_s = 0$). (a) Critical Péclet number Pe_c as a function of flow strength ξ in the $k' = 0$ limit for a wave in the flow direction $\Theta = 0$. (b) Pe_c as a function of Θ ($k' = 0$). (c) Influence of ξ in the system threshold size (critical wavenumber k_c').

the influence of the flow on the system threshold size criterion, generalizing the results of Fig. 2.1b to non-zero ξ values. Interestingly, we notice that *small values of* $|\xi|$ *may actually slightly destabilize the smallest systems* and that *the function* $Pe = Pe(k_c)$ *may no longer be monotonic*, especially for large values of $|\xi|$. Note that this does not mean that larger systems may be more stable than smaller ones (assuming that a system of size L has random perturbations of all wavelengths $\leq \sqrt{2}L$), but rather that the instabilities may develop at smaller scales.

2.3 Nearly uniform and aligned suspension

2.3.1 Reduced equations in the aligned case

To address the stability around the aligned steady state, we consider a distribution function of the form

$$\Psi(\mathbf{x}, \mathbf{p}, t) = c(\mathbf{x}, t)\delta(\mathbf{p} - \mathbf{P}(\mathbf{x}, t)), \tag{2.42}$$

where δ is the Dirac delta function. This simple $\mathbf{p}$-dependence (separation of variables) is very helpful in the modeling of suspensions where a single polarization $\mathbf{P}$ at a given location may be assumed. Using this closure relation, our objective is to derive equations for the concentration and polarization fields.

It is clear from the continuity equation Eq. (1.7) that rotational diffusion makes the uniform and aligned state unsteady, hence we set $D_R = 0$ to study the stability of this state. The evolution of c is then simply obtained by integrating Eq. (1.7) with respect to $\mathbf{p}$ on the unit circle:

$$\begin{aligned}
\frac{\partial c}{\partial t} = \int \frac{\partial \Psi}{\partial t}\, \mathrm{d}\mathbf{p} &= \int \Big(-\nabla\cdot(\Psi\,\dot{\mathbf{R}}) - \nabla_{\mathbf{p}}\cdot(\Psi\,\dot{\mathbf{p}}) + D\,\nabla^2\Psi \Big)\, \mathrm{d}\mathbf{p} \\
&= -\nabla\cdot\int c\,\delta(\mathbf{p}-\mathbf{P})\Big(v_s\mathbf{p} + \mu_\perp\mathbf{u} + (\mu_\parallel - \mu_\perp)\mathbf{p}\mathbf{p}\cdot\mathbf{u}\Big)\, \mathrm{d}\mathbf{p} + D\,\nabla^2\int \Psi\, \mathrm{d}\mathbf{p} \\
&= -\nabla\cdot\Big[c\Big(v_s\mathbf{P} + \mu_\perp\mathbf{u} + (\mu_\parallel - \mu_\perp)\mathbf{P}\mathbf{P}\cdot\mathbf{u}\Big)\Big] + D\nabla^2 c.
\end{aligned} \tag{2.43}$$

Similarly, we derive an evolution equation for $c\mathbf{P} = \int \Psi \mathbf{p}\, \mathrm{d}\mathbf{p}$ as follows:

$$\begin{aligned}\frac{\partial (c\mathbf{P})}{\partial t} &= -\nabla \cdot \int c\,\delta(\mathbf{p}-\mathbf{P})\Big(v_s\mathbf{p} + \mu_\perp \mathbf{u} + (\mu_\parallel - \mu_\perp)\mathbf{p}\mathbf{p}\cdot\mathbf{u}\Big)\mathbf{p}\,\mathrm{d}\mathbf{p} \\ &\quad - \int \mathbf{p}\nabla_{\mathbf{p}} \cdot \Big[c\,\delta(\mathbf{p}-\mathbf{P})\Big(\nu(\mathbf{I}-\mathbf{p}\mathbf{p})\cdot\mathbf{u} + \nu'(\mathbf{I}-\mathbf{p}\mathbf{p})\cdot\nabla\mathbf{u}\cdot\mathbf{p}\Big)\Big]\,\mathrm{d}\mathbf{p} + D\,\nabla^2 \int \Psi\mathbf{p}\,\mathrm{d}\mathbf{p} \\ &= -\nabla\cdot\Big[c\Big(v_s\mathbf{P} + \mu_\perp\mathbf{u} + (\mu_\parallel-\mu_\perp)\mathbf{P}\mathbf{P}\cdot\mathbf{u}\Big)\mathbf{P}\Big] \\ &\quad + c\Big(\nu(\mathbf{I}-\mathbf{P}\mathbf{P})\cdot\mathbf{u} + \nu'(\mathbf{I}-\mathbf{P}\mathbf{P})\cdot\nabla\mathbf{u}\cdot\mathbf{P}\Big) + D\,\nabla^2(c\mathbf{P}). \end{aligned} \tag{2.44}$$

where we used integration by parts for the second integral. Expanding the derivatives yields

$$\begin{aligned}\mathbf{P}\frac{\partial c}{\partial t} + c\frac{\partial \mathbf{P}}{\partial t} = -\mathbf{P}\,\nabla\cdot\Big[c\Big(v_s\mathbf{P}+\mu_\perp\mathbf{u}+(\mu_\parallel-\mu_\perp)\mathbf{P}\mathbf{P}\cdot\mathbf{u}\Big)\Big] - c\Big(v_s\mathbf{P}+\mu_\perp\mathbf{u}+(\mu_\parallel-\mu_\perp)\mathbf{P}\mathbf{P}\cdot\mathbf{u}\Big)\nabla\cdot\mathbf{P} \\ + c\Big(\nu(\mathbf{I}-\mathbf{P}\mathbf{P})\cdot\mathbf{u} + \nu'(\mathbf{I}-\mathbf{P}\mathbf{P})\cdot\nabla\mathbf{u}\cdot\mathbf{P}\Big) + D\,(\mathbf{P}\nabla^2 c + 2\nabla c\cdot\nabla\mathbf{P} + c\nabla^2\mathbf{P}),\end{aligned} \tag{2.45}$$

We now make use of Eq. (2.43) to deduce an equation for $\mathbf{P}$

$$\frac{\partial \mathbf{P}}{\partial t} = -\Big(v_s\mathbf{P}+\mu_\perp\mathbf{u}+(\mu_\parallel-\mu_\perp)\mathbf{P}\mathbf{P}\cdot\mathbf{u}\Big)\nabla\cdot\mathbf{P} + (\mathbf{I}-\mathbf{P}\mathbf{P})\cdot(\nu\mathbf{u}+\nu'\nabla\mathbf{u}\cdot\mathbf{P}) + D\Big(2\frac{\nabla c}{c}\cdot\nabla\mathbf{P} + \nabla^2\mathbf{P}\Big). \tag{2.46}$$

2.3.2 Linearization

We consider a suspension with an initial uniform concentration c_0 and alignment $\hat{\mathbf{x}}$. This stationary solution is slightly perturbed as follows:

$$c(\mathbf{x},t) = c_0(1+\varepsilon c'(\mathbf{x},t)) \quad \text{and} \quad \mathbf{P}(\mathbf{x},t) = \hat{\mathbf{x}} + \varepsilon\mathbf{P}'(\mathbf{x},t), \tag{2.47}$$

where $|\hat{\mathbf{x}}| = 1$, $\mathbf{P}'\cdot\hat{\mathbf{x}} = 0$ and we assume similar perturbations for the velocity and pressure fields: $\mathbf{u}(\mathbf{x},t) = \varepsilon\mathbf{u}'(\mathbf{x},t)$ and $\Pi(\mathbf{x},t) = \varepsilon\Pi'(\mathbf{x},t)$. Using the reduced equations Eqs. (2.43), (2.46) we aim at obtaining a set of linearized equations for the perturbation variables c' and $\mathbf{P}'$ valid in the $|\varepsilon| \ll 1$ limit. We therefore start by plugging Eq. (2.47) into Eq. (2.43)

$$\begin{aligned}c_0\frac{\partial(1+\varepsilon c')}{\partial t} &= -c_0\nabla\cdot\Big[(1+\varepsilon c')\Big(v_s(\hat{\mathbf{x}}+\varepsilon\mathbf{P}')+\mu_\perp\varepsilon\mathbf{u}'+(\mu_\parallel-\mu_\perp)(\hat{\mathbf{x}}+\varepsilon\mathbf{P}')(\hat{\mathbf{x}}+\varepsilon\mathbf{P}')\cdot\varepsilon\mathbf{u}'\Big)\Big] + D\nabla^2(1+\varepsilon c') \\ &= -c_0\nabla\cdot\Big(\varepsilon c' v_s\hat{\mathbf{x}} + v_s\varepsilon\mathbf{P}' + \mu_\perp\varepsilon\mathbf{u}' + (\mu_\parallel-\mu_\perp)\hat{\mathbf{x}}\hat{\mathbf{x}}\cdot\varepsilon\mathbf{u}'\Big) + Dc_0\nabla^2(\varepsilon c') + \mathcal{O}(\varepsilon^2),\end{aligned} \tag{2.48}$$

which, at leading order in ε, reduces to

$$\frac{\partial c'}{\partial t} = -v_s(\nabla c'\cdot\hat{\mathbf{x}} + \nabla\cdot\mathbf{P}') - \mu_\perp\nabla\cdot\mathbf{u}' - (\mu_\parallel-\mu_\perp)\nabla\mathbf{u}' : \hat{\mathbf{x}}\hat{\mathbf{x}} + D\nabla^2 c'. \tag{2.49}$$

Similarly, plugging Eq. (2.47) into Eq. (2.46), we obtain

$$\begin{aligned}\frac{\partial(\hat{\mathbf{x}}+\varepsilon\mathbf{P}')}{\partial t} &= -\Big(v_s(\hat{\mathbf{x}}+\varepsilon\mathbf{P}') + \mu_\perp\varepsilon\mathbf{u}' + (\mu_\parallel-\mu_\perp)(\hat{\mathbf{x}}+\varepsilon\mathbf{P}')(\hat{\mathbf{x}}+\varepsilon\mathbf{P}')\cdot\varepsilon\mathbf{u}'\Big)\nabla\cdot(\hat{\mathbf{x}}+\varepsilon\mathbf{P}') \\ &\quad + \Big(\mathbf{I}-(\hat{\mathbf{x}}+\varepsilon\mathbf{P}')(\hat{\mathbf{x}}+\varepsilon\mathbf{P}')\Big)\cdot\Big(\nu\varepsilon\mathbf{u}' + \nu'\varepsilon\nabla\mathbf{u}'\cdot(\hat{\mathbf{x}}+\varepsilon\mathbf{P}')\Big) \\ &\quad + 2D\frac{\nabla(1+\varepsilon c')}{1+\varepsilon c'}\cdot\nabla(\hat{\mathbf{x}}+\varepsilon\mathbf{P}') + D\nabla^2(\hat{\mathbf{x}}+\varepsilon\mathbf{P}') \\ &= -v_s\hat{\mathbf{x}}\nabla\cdot(\varepsilon\mathbf{P}') + (\mathbf{I}-\hat{\mathbf{x}}\hat{\mathbf{x}})\cdot(\nu\varepsilon\mathbf{u}' + \nu'\varepsilon\nabla\mathbf{u}'\cdot\hat{\mathbf{x}}) + D\nabla^2(\varepsilon\mathbf{P}') + \mathcal{O}(\varepsilon^2),\end{aligned} \tag{2.50}$$

or, at leading order in ε

$$\frac{\partial \mathbf{P}'}{\partial t} = -v_s \nabla \cdot \mathbf{P}' \ \hat{\mathbf{x}} + (\mathbf{I} - \hat{\mathbf{x}}\hat{\mathbf{x}}) \cdot (\nu \mathbf{u}' + \nu' \nabla \mathbf{u}' \cdot \hat{\mathbf{x}}) + D\nabla^2 \mathbf{P}'. \tag{2.51}$$

We must now find a relation between $\mathbf{u}'$ and $c', \mathbf{P}'$. Recalling Eqs. (2.8a)-(2.8c), we write

$$\begin{aligned} \nabla \cdot \mathbf{u} &= -\sigma \ \nabla \cdot \Big[c\Big(v_s \mathbf{P} + (\mu_\perp - 1)\mathbf{u} + (\mu_\parallel - \mu_\perp)\mathbf{P}\mathbf{P} \cdot \mathbf{u} \Big) \Big] \\ &= -\sigma c_0 \ \nabla \cdot \Big[(1 + \varepsilon c') \Big(v_s (\hat{\mathbf{x}} + \varepsilon \mathbf{P}') + (\mu_\perp - 1)\varepsilon \mathbf{u}' + (\mu_\parallel - \mu_\perp)(\hat{\mathbf{x}} + \varepsilon \mathbf{P}')(\hat{\mathbf{x}} + \varepsilon \mathbf{P}') \cdot \varepsilon \mathbf{u}' \Big) \Big], \end{aligned} \tag{2.52}$$

from which we deduce the following expression for the perturbation velocity:

$$\nabla \cdot \mathbf{u}' = -\sigma c_0 v_s \ \nabla \cdot (c' \hat{\mathbf{x}} + \mathbf{P}') - \sigma c_0 \Big((\mu_\perp - 1) \nabla \cdot \mathbf{u}' + (\mu_\parallel - \mu_\perp) \nabla \mathbf{u}' : \hat{\mathbf{x}}\hat{\mathbf{x}} \Big). \tag{2.53}$$

We can get a simple expression for $\nabla \cdot \mathbf{u}'$ making the assumption that the anisotropy of our swimmers is small enough[2] to neglect the term in $\nabla \mathbf{u}'$. Under this $\tilde{\mu} \approx 0$ approximation (i.e. $\mu_\perp, \mu_\parallel \approx \bar{\mu}$) we have

$$\nabla \cdot \mathbf{u}' = -f v_s (\nabla c' \cdot \ \hat{\mathbf{x}} + \nabla \cdot \mathbf{P}'). \tag{2.54}$$

where f, the corrected volume fraction, is defined in Eq. (2.11).

2.3.3 Fourier transform and eigenvalue problem

Assuming that the perturbations take the form of plane waves, it is natural to study the two linear equations Eqs. (2.49), (2.51) in the Fourier space

$$c'(\mathbf{x}, t) = \tilde{c}(\mathbf{k}, \hat{\mathbf{x}}) \exp(i\mathbf{k} \cdot \mathbf{x} + \alpha t) \quad \text{and} \quad \mathbf{P}'(\mathbf{x}, t) = \tilde{\mathbf{P}}(\mathbf{k}, \hat{\mathbf{x}}) \exp(i\mathbf{k} \cdot \mathbf{x} + \alpha t), \tag{2.55}$$

where $\tilde{c}, \tilde{\mathbf{P}}$ are the Fourier amplitudes ($\mathbf{u}'$ and Π' take the same form). We can then use Eq. (2.54) to find the Fourier amplitudes of $\nabla \cdot \mathbf{u}'$, $\mathbf{u}'$ and $\nabla \mathbf{u}'$, successively:

$$\widetilde{\nabla \cdot \mathbf{u}'} = -ikfv_s(\tilde{c}\hat{\mathbf{k}} \cdot \hat{\mathbf{x}} + \tilde{\mathbf{P}} \cdot \hat{\mathbf{k}}), \tag{2.56a}$$

$$\widetilde{\mathbf{u}'} = -fv_s \Big(\tilde{c}(\hat{\mathbf{k}} \cdot \hat{\mathbf{x}})\hat{\mathbf{k}} + (\tilde{\mathbf{P}} \cdot \hat{\mathbf{k}})\hat{\mathbf{k}} \Big), \tag{2.56b}$$

$$\widetilde{\nabla \mathbf{u}'} = -ikfv_s \Big(\tilde{c}(\hat{\mathbf{k}} \cdot \hat{\mathbf{x}})\hat{\mathbf{k}}\hat{\mathbf{k}} + (\tilde{\mathbf{P}} \cdot \hat{\mathbf{k}})\hat{\mathbf{k}}\hat{\mathbf{k}} \Big), \tag{2.56c}$$

where use has been made of the fact that $\mathbf{u}'$ is potential as in Eq. (2.14). It is now possible to rewrite Eqs. (2.49), (2.51) in terms of Fourier amplitudes

$$\begin{aligned} \alpha \tilde{c} &= -ikv_s(\tilde{c}\hat{\mathbf{k}} \cdot \hat{\mathbf{x}} + \tilde{\mathbf{P}} \cdot \hat{\mathbf{k}}) + ikv_s f \mu_\perp (\tilde{c}\hat{\mathbf{k}} \cdot \hat{\mathbf{x}} + \tilde{\mathbf{P}} \cdot \hat{\mathbf{k}}) \\ &\quad + ikv_s f(\mu_\parallel - \mu_\perp) \Big(\tilde{c}(\hat{\mathbf{k}} \cdot \hat{\mathbf{x}})\hat{\mathbf{k}}\hat{\mathbf{k}} : \hat{\mathbf{x}}\hat{\mathbf{x}} + (\tilde{\mathbf{P}} \cdot \hat{\mathbf{k}})\hat{\mathbf{k}}\hat{\mathbf{k}} : \hat{\mathbf{x}}\hat{\mathbf{x}} \Big) - Dk^2 \tilde{c}, \end{aligned} \tag{2.57a}$$

$$\begin{aligned} \alpha \tilde{\mathbf{P}} &= -ikv_s(\tilde{\mathbf{P}} \cdot \hat{\mathbf{k}})\hat{\mathbf{x}} - fv_s(\mathbf{I} - \hat{\mathbf{x}}\hat{\mathbf{x}}) \Big[\nu \Big(\tilde{c}(\hat{\mathbf{k}} \cdot \hat{\mathbf{x}})\hat{\mathbf{k}} + (\tilde{\mathbf{P}} \cdot \hat{\mathbf{k}})\hat{\mathbf{k}} \Big) \\ &\quad + ik\nu' \Big(\tilde{c}(\hat{\mathbf{k}} \cdot \hat{\mathbf{x}})\hat{\mathbf{k}}\hat{\mathbf{k}} \cdot \hat{\mathbf{x}} + (\tilde{\mathbf{P}} \cdot \hat{\mathbf{k}})\hat{\mathbf{k}}\hat{\mathbf{k}} \cdot \hat{\mathbf{x}} \Big) \Big] - Dk^2 \tilde{\mathbf{P}}. \end{aligned} \tag{2.57b}$$

[2] This is consistent with our aim to focus on the influence of polarity (parameter ν) on stability. As previously mentionned, the instabilities associated with the (probably similar) effects of $\nu' \neq 0$ have been studied by Caussin [18].

Let us define in whole generality $\theta = \cos^{-1}(\hat{\mathbf{x}}\cdot\hat{\mathbf{k}})$ and recall that $\tilde{\mathbf{P}} \perp \hat{\mathbf{x}}$ such that $\tilde{\mathbf{P}}\cdot\hat{\mathbf{k}} = \tilde{P}\sin\theta$. Eqs. (2.57a), (2.57b) hence take the following scalar form

$$\begin{aligned}(\alpha + k^2 D)\tilde{c} &= ikv_s\Big(-(\tilde{c}\cos\theta + \tilde{P}\sin\theta) + f\mu_\perp(\tilde{c}\cos\theta + \tilde{P}\sin\theta) \\ &\quad + f(\mu_\parallel - \mu_\perp)(\tilde{c}\cos^3\theta + \tilde{P}\sin\theta\cos^2\theta)\Big) \qquad (2.58a)\\ (\alpha + k^2 D)\tilde{P}\sin\theta &= -ikv_s(\tilde{\mathbf{P}}\cdot\hat{\mathbf{k}})\hat{\mathbf{x}}\cdot\hat{\mathbf{k}} - fv_s\Big((\mathbf{I} - \hat{\mathbf{x}}\hat{\mathbf{x}}) : \hat{\mathbf{k}}\hat{\mathbf{k}}\Big)\Big[\nu\Big(\tilde{c}(\hat{\mathbf{k}}\cdot\hat{\mathbf{x}}) + (\tilde{\mathbf{P}}\cdot\hat{\mathbf{k}})\Big) \\ &\quad + \nu' ik\Big(\tilde{c}(\hat{\mathbf{k}}\cdot\hat{\mathbf{x}})\hat{\mathbf{k}}\cdot\hat{\mathbf{x}} + (\tilde{\mathbf{P}}\cdot\hat{\mathbf{k}})\hat{\mathbf{k}}\cdot\hat{\mathbf{x}}\Big)\Big] \\ &= -ikv_s\tilde{P}\sin\theta\cos\theta - fv_s\sin^2\theta\Big(\nu(\tilde{c}\cos\theta + \tilde{P}\sin\theta) \\ &\quad + \nu' ik(\tilde{c}\cos^2\theta + \tilde{P}\sin\theta\cos\theta)\Big). \qquad (2.58b)\end{aligned}$$

Anticipating on our results, we notice that $\theta = 0$ and $\theta = \pi$ perturbations (for which $\hat{\mathbf{k}} \parallel \hat{\mathbf{x}}$) are stable (as expected), so that we shall not investigate these cases further and therefore divide Eq. (2.58b) by $\sin\theta$. It further proves convenient to scale the growth rate as: $\alpha' = (\alpha + k^2 D)/v_s$ (with dimension $[\alpha'] = [k] = L^{-1}$), and by doing that, we acknowledge the fact that the translational diffusion D simply increases stability at high k. In matrix form, the eigenvalue problem Eqs. (2.58a), (2.58b) yields

$$\alpha'\begin{pmatrix}\tilde{c}\\ \tilde{P}\end{pmatrix} = \begin{pmatrix}-ik\cos\theta\Big(1 - f(\mu_\parallel\cos^2\theta + \mu_\perp\sin^2\theta)\Big) & -ik\sin\theta\Big(1 - f(\mu_\parallel\cos^2\theta + \mu_\perp\sin^2\theta)\Big)\\ -\frac{1}{2}f\sin 2\theta(\nu + ik\nu'\cos\theta) & -ik\cos\theta - f\sin^2\theta(\nu + ik\nu'\cos\theta)\end{pmatrix}\cdot\begin{pmatrix}\tilde{c}\\ \tilde{P}\end{pmatrix}, \qquad (2.59)$$

or, following the notations introduced in Eq. (2.22)

$$\alpha'\begin{pmatrix}\tilde{c}\\ \tilde{P}\end{pmatrix} = -ik\begin{pmatrix}\cos\theta(1 - \bar{H} + \frac{1}{2}\widetilde{H}\cos 2\theta) & \sin\theta(1 - \bar{H} + \frac{1}{2}\widetilde{H}\cos 2\theta)\\ \frac{1}{2}\sin 2\theta(-i\frac{f\nu}{k} + f\nu'\cos\theta) & \cos\theta + \sin^2\theta(-i\frac{f\nu}{k} + f\nu'\cos\theta)\end{pmatrix}\cdot\begin{pmatrix}\tilde{c}\\ \tilde{P}\end{pmatrix}. \qquad (2.60)$$

Two special cases of this problem may easily be solved analytically. First, in the long-wavelength limit $k \to 0$, the non-zero eigenvalue of the system Eq. (2.60) is

$$\alpha' = -f\nu\sin^2\theta, \qquad (2.61)$$

with a unstable mode involving pure polarization ($\tilde{c} = 0$). In this case, perturbations normal to the initial direction ($\theta = \pi/2$) are (quite intuitively) the most unstable. Second, for $\theta = \pi/2$ perturbations, it is straightforward to show that

$$\alpha' = -f\nu, \qquad (2.62)$$

regardless of the wavenumber k, with a complex mode $\tilde{c} = [ik(1-\bar{H})/f\nu]\tilde{P}$. This result will be especially relevant for large-heads, where $\theta = \pi/2$ is often close to the most unstable angle as we will discuss next.

2.3.4 Large-head instability

To start with, Eq. (2.61) means that the polarization of large-heads ($\nu < 0$) is unstable to long-wavelength perturbations and tends to grow perpendicular to the main direction. Eq. (2.62) focuses on $\pi/2$ perturbations but catches the k-dependence and suggests that such perturbations result in a growth rate

$\alpha = -v_s f\nu - k^2 D$, that increases with the swimming speed, surface fraction and polarity. Most interestingly, opposite phase concentration fluctuations are found for finite k/ν ratios. Specifically, this occurs when the perturbation wavelength λ becomes of the order of magnitude of the length of a dumbbell swimmer a (since $k/\nu \sim a/\lambda$)[3]. In short, these two simple results enable us to conclude that the concentration and polarization of large-head suspensions are unstable, probably mostly to $\theta = \pi/2$ waves and that the role of the ratio between the length of particles and the wavelength needs further investigation.

Let us now try to understand the instability associated to $\pi/2$ perturbations with simple physical arguments, as done in [18]. Fig. 2.4 depicts large-head dumbbells swimming in the x direction and experiencing short wavelength ($\lambda \approx a$), opposite phase perturbations in concentration δc and polarization $\delta\mathbf{P}$. First, δc makes swimmer 2 closer from the central one (swimmer 1). The dipolar flow from swimmer 2 thus induces at the swimmer 1 location a velocity of higher intensity (red arrow) than the flow from swimmer 3 (blue arrow), resulting in a net velocity along $-y$. Second, $\delta\mathbf{P}$ along y makes swimmer 4 induce an additional velocity perturbation, also along $-y$ (green arrow), resulting in a total net flow $\delta\mathbf{u}$ along $-y$. As swimmer 1 tends to reorient against $\delta\mathbf{u}$ according to $\dot{\mathbf{p}} = \nu(\mathbf{I} - \mathbf{pp})\cdot\delta\mathbf{u} = \nu\delta\mathbf{u} + \mathcal{O}(\varepsilon^3)$ with $\nu < 0$, the initial $\delta\mathbf{P}$ increases with time. Since swimmer 1 now tends to self-propel along y, the initially higher concentration in this region increases, triggering the growth of δc and explaining the coupling of $\tilde{c}$ and $\tilde{P}$ at this scale of finite k/ν ratios. Note that the exact same argument with $\nu > 0$ confirms that large-tails are stable to such waves.

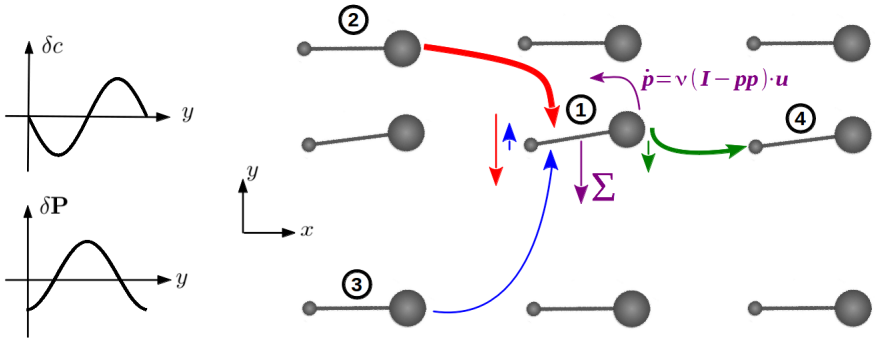

FIG. 2.4: Instability mechanism of a large-head nearly aligned suspension. Short wavelength, perpendicular and opposite phase perturbations in concentration and polarization δc, $\delta\mathbf{P}$ result in a net flow for the central swimmer (1), which tends to reorient against it, increasing $\delta\mathbf{P}$ and hence δc.

Solving the eigenvalue problem numerically enables us to gain more insight into the behavior of the system under more general perturbations ($k \neq 0$ or $\theta \neq \pi/2$) when simple physical considerations are lacking. Fig. 2.5a shows the positive real growth rate with respect to θ for various k, while Fig. 2.5b shows it with respect to k for various θ (here $\nu = -1$). They first show that small wavelength perturbations grow faster, suggesting a small-scale destruction of this ordered state (recall that a maximum for $\alpha = v_s\alpha' - k^2 D$ is actually expected for finite D because of the superimposed $\sim -k^2$ parabolic behavior). These figures

[3]Keep in mind that the continuum approximation and the dilute limite require that $\lambda \gg a$, hence $k/\nu \ll 1$.

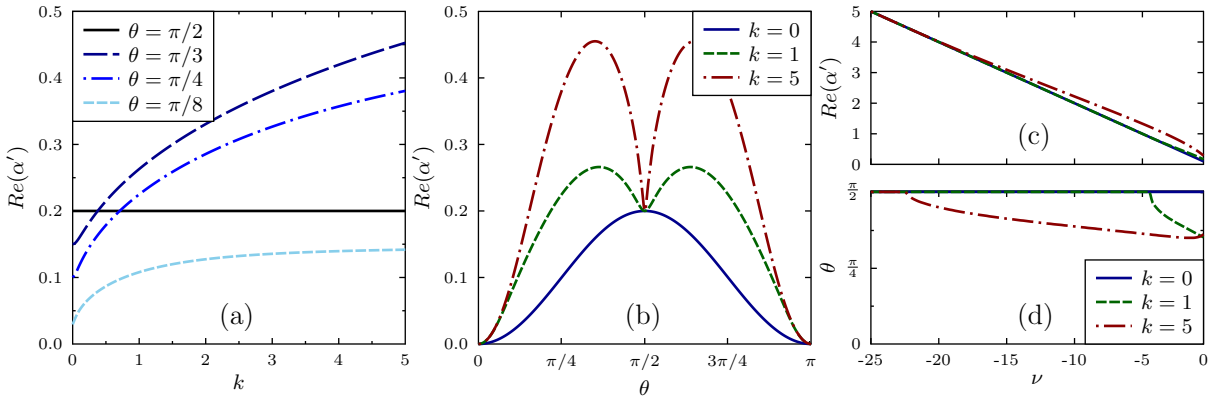

FIG. 2.5: Instability of aligned large-head swimmers. (a) $Re(\alpha')$ as a function of k for various θ and (b) as a function of θ for various k. Parameters used: $\nu = -1$, $f = \bar{H} = 0.2$, $\widetilde{H} = 0$. (c) Maximum $Re(\alpha')$ as a function of ν and (d) angle θ at which it is attained (same $f, \bar{H}, \widetilde{H}$ used).

also prove that for $k \neq 0$, the system may indeed be most unstable to non-perpendicular perturbations (note the symmetry about $\pi/2$). Fig. 2.5c shows the maximum $Re(\alpha')$ as a function of ν for various k and Fig. 2.5d the angle θ at which it is attained. We see that $\theta \approx 3\pi/8$ is the most unstable angle for $\nu \to 0$, whereas $\pi/2$ becomes most unstable for $\nu < -\beta k$, where we found that β is a decreasing function of $\bar{H}$ (here $\beta \approx 4.5$). More interestingly, we notice in Fig. 2.5c that α' converges very fast to the $-f\nu$ limit found in Eq. (2.62). This means that even when the maximum growth rate is not attained at $\pi/2$, the $\pi/2$ value derived analytically remains an excellent approximation. The analysis further revealed that the unstable complex modes generally combine concentration and polarization. Eventually, we found that $|Im(\alpha')|$ is maximum for $\theta \approx 0$ perturbations (the most stable ones) but that its value remains large everywhere (except for $\theta \approx \pi/2$ where $Im(\alpha') = 0$). We thus expect every $\theta \neq \pi/2$ instabilities to give rise to travelling waves.

2.3.5 Large-tail instability

Although the previous analytical limits (Eq. (2.61) for $k = 0$ and Eq. (2.62) for $\theta = \pi/2$) do *not* suggest instability for $\nu > 0$, numerical solutions revealed that suspensions of large-tails *are* unstable to certain perturbations. Fig. 2.6a and Fig. 2.6b show that small scale fluctuations are again the most unstable, although they are characterized by much lower growth rates than large-heads (see in particular Fig. 2.6c, where the scale of $Re(\alpha')$ has been made identical to that of Fig. 2.5c for comparison). Note that in contrast with the previous case where $\theta \approx \pi/2$ fluctuations were dominant, these systems are surprisingly most sensitive to angles $\pi/8 < \theta < \pi/4$, as shown in Fig. 2.5d. In addition, as in the large-head case, this instability always couples concentration and polarization and $Im(\alpha') \neq 0$ for $\theta \neq \pi/2$ perturbations, hence we predict travelling waves. Eventually, we found that the qualitative features of theses results are relatively independent of f, $\bar{H}$ and $\widetilde{H}$.

To conclude this chapter, we should remember that the whole analysis did not emphasize the effect

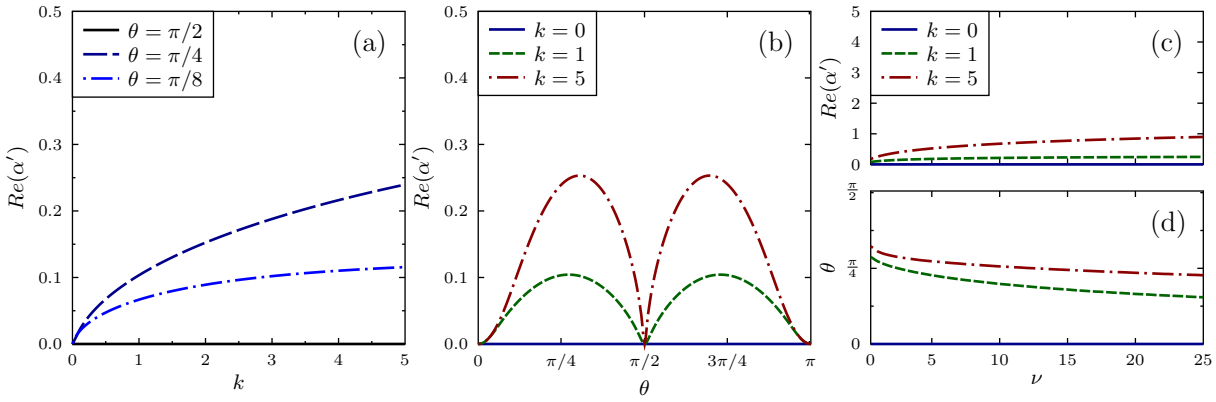

FIG. 2.6: Instability of aligned large-tail swimmers. (a) $Re(\alpha')$ as a function of k for various θ and (b) as a function of θ for various k. Parameters used: $\nu = 1,\ f = \bar{H} = 0.1,\ \widetilde{H} = 0$. (c) Maximum $Re(\alpha')$ as a function of ν and (d) angle θ at which it is attained (same $f, \bar{H}, \widetilde{H}$ used).

of the anisotropy of swimmers $(\tilde{\mu}, \nu')$. A previous stability analysis of the aligned base state focused on the role of ν' and concluded that this parameter alone can also cause small scale instability near the $\theta = \pi/2$ region [18]. We therefore conclude that both anisotropy[4] and polarity destabilize this ordered state, probably at the smallest scale of the system, i.e. the scale of inter-particle distance. It is therefore obvious that *no natural system can actually reach this homogeneous and aligned state on a large scale*, which is the reason why we shall not investigate this case further. By constrast, we concluded in the previous section that *isotropic* large-head suspensions were unstable to *long-wavelength* perturbations that is, *large-scale collective motion* is predicted *only above a critical system size*. Obviously, this conclusion is of paramount interest for biological colonies and this explains why the next chapter is exclusively devoted to the elucidation of such phenomena by means of numerical simulation.

[4]Since ν' appears only with $\tilde{\mu}$ in $\widetilde{H} = f(\tilde{\mu} + 2\nu')$ we consider that these two anisotropic parameters have the same effect.

Chapter 3

Nonlinear numerical simulations

3.1 Direct particle simulation method

To start with, let us introduce the basic features of the direct particle simulaion code used troughout this chapter to investigate the long-time nonlinear dynamics of confined suspensions.

The code we developed aims at studying the time evolution of a *2D, initially isotropic suspension of polar swimmers*. For this purpose, the program handles the position $\mathbf{R}_i^n$, orientation $\mathbf{p}_i^n$ and dipole moment $\boldsymbol{\sigma}_i^n$ of M particles ($i = 1, ..., M$ refers to particles while $n = 1, ..., N$ denotes the time step). Positions are randomly initialized following a uniform law: $R_{xi}^0 \sim \mathcal{U}([-LX/2, LX/2])$ and $R_{yi}^0 \sim \mathcal{U}([-LY/2, LY/2)]$ in the computational domain (a rectangular box of dimensions LX, LY). Similarly, orientation vectors are randomized using the θ angle to guarantee anisotropy: $(p_{xi}^0, p_{yi}^0) = (\cos\theta_i^0, \sin\theta_i^0)$ where $\theta_i^0 \sim \mathcal{U}([0, 2\pi]))$ and dipole moments are initialized as follows: $\boldsymbol{\sigma}_i^0 = \sigma v_s \mathbf{p}_i^0$. Most simulations were carried out in a square box ($LX = LY = L$) assuming *periodic boundary conditions*, to model an infinite system with *no boundary in x or y*. This classical type of boundary conditions naturally requires the introduction of a set of *image particles* (hereafter referred to as *periodic images*). As illustrated in Fig. 3.1, these N_{img} images are simply deduced from the M actual particles by $\pm L$ translations along x and y.

More specifically, at each time step n, the fluid flow at the location of a given particle i is computed by summing all the individual dipolar interactions due to the $M-1$ other particles inside the computational box and all $M[(2N_{img}+1)^2 - 1]$ periodic images

$$\mathbf{u}(\mathbf{R}_i^n) = \Bigg[\underbrace{\sum_{\substack{j=1 \\ j\neq i}}^{M} \mathbf{G}(\mathbf{R}_{ij}^n)}_{M-1 \text{ real particles}} + \underbrace{\sum_{j=1}^{M} \Big(\sum_{\substack{p=-N_{img} \\ p\neq 0}}^{N_{img}} \sum_{\substack{q=-N_{img} \\ q\neq 0}}^{N_{img}} \mathbf{G}(\mathbf{R}_{ij}^n + pL\mathbf{e}_x + qL\mathbf{e}_y) \Big)}_{N_{img} \text{ periodic images in } x \text{ and } y.\ \text{Total: } M[(2N_{img}+1)^2-1].} \Bigg] \cdot \boldsymbol{\sigma}_j^n, \tag{3.1}$$

where $\mathbf{e}_x, \mathbf{e}_y$ are the cartesian unit vectors, $\mathbf{R}_{ij}^n = \mathbf{R}_i^n - \mathbf{R}_j^n$ and the Green tensor $\mathbf{G}$ takes the following form (see Eq. (1.3)):

$$\mathbf{G}(\mathbf{R}) = \frac{1}{2\pi|\mathbf{R}|^2}\Big(2\frac{\mathbf{RR}}{|\mathbf{R}|^2} - \mathbf{I}\Big). \tag{3.2}$$

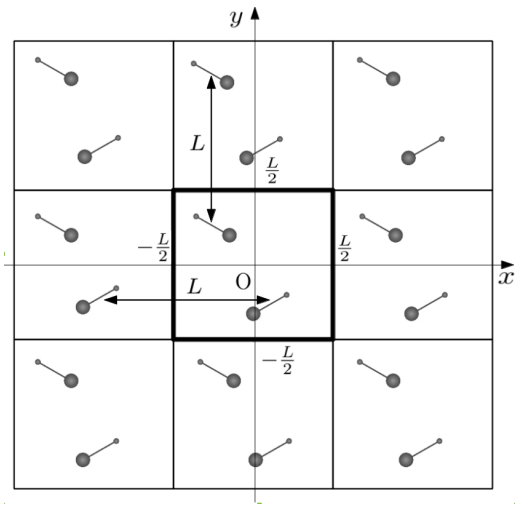

FIG. 3.1: Image system for periodic BC in a square box of size L. $M = 2$ particles in the computational domain $[-L/2, L/2]^2$ (bold line) are represented with $N_{img} = 1$ image in each direction located at $(R_{xi} \pm L, R_{yi} \pm L)$.

Given $\mathbf{u}(\mathbf{R}_i^n)$, particle i is then advanced in time following the equations of motion of a single swimmer immersed in an arbitrary flow field Eqs. (1.4a), (1.4b) using a fourth-order Runge-Kutta (RK4) time marching scheme. Rotational diffusion is included by adding to the orientational dynamics $\dot{\mathbf{p}}$ the following stochastic vector: $\sqrt{2D_R/dt}\,(\mathbf{I} - \mathbf{pp})\cdot\mathbf{n}$ where dt is the time increment and $n_i \sim \mathcal{N}(0,1)$ are two Gaussian-distributed independent components. For relatively large values of D_R (to overcome natural diffusion due to interactions), we found the following relations for orientational and translation time autocorrelation:

$$\frac{1}{N}\sum_{i=1}^{M} \mathbf{p}_i(t)\cdot\mathbf{p}_i(0) = \exp(-D_R t) \qquad \text{and} \qquad \frac{1}{N}\sum_{i=1}^{M} |\mathbf{R}_i(t) - \mathbf{R}_i(0)|^2 = \frac{2v_s^2}{D_R}t = 4Dt, \tag{3.3}$$

which can be shown to be in full agreement with their role of diffusion coefficients in the continuous 2D Smoluchowski equation (more generally, these relations hold when t and 0 are replaced respectively by $t + \tau$ and t for $\tau \gg 1$). This equivalence of diffusion coefficients in both models will prove important to compare simulation results with predictions from the kinetic model. Eventually, dipole moments are updated as follows: $\boldsymbol{\sigma}_i^{n+1} = \sigma[\dot{\mathbf{R}}_i^n - \mathbf{u}(\mathbf{R}_i^n)]$. Note that in this expression, both the particle velocity and the fluid velocity are necessarily evaluated at time step n, which essentially results in approximating $\boldsymbol{\sigma}_i^{n+1}$ by $\boldsymbol{\sigma}_i^n$. Although this preserves the consistency of the scheme, we hope to control this source of error with the excellent properties of the RK4 scheme (within each time step, $\mathbf{u}, \dot{\mathbf{R}}, \dot{\mathbf{p}}$ are evaluated four times and $\boldsymbol{\sigma}$ updated accordingly) and by setting a conservative time increment dt. We indeed choose dt such that a particle swimming at speed v_s during dt travels less that 10% of the average distance separating two particles $\sqrt{L^2/M}$: $dt < L/(10v_s\sqrt{M})$.

Most simulations were typically carried out with $N_{img} = 200$ images in each directions (x and y) for greater accuracy, though convergence has been observed for lower values of N_{img}. In theory, this would require the computation of $4M[(2N_{img}+1)^2 - 1] \approx 6 \times 10^5 M$ interactions to get the velocity at a single particle location (hence $6 \times 10^5 M^2$ at each time step). It follows that simulating systems

with thousands of swimmers on a single-processor workstation is only possible provided that we use an accelerated algorithm, which we shall briefly introduce. The general philosophy behind most accelerated algorithms is to evaluate directly the largest interactions, and approximate the far-field ones. We applied this idea to compute the sum of interactions due to particle j and all its images with particle i, using the following algorithm:

- Search the closest particle to i among j and its first 8 images (inside all adjacent boxes, see Fig. 3.1). In other words, find $\mathbf{R}_{ij}^{min}$, the vector $\mathbf{R}_{ij} + pL\mathbf{e}_x + qL\mathbf{e}_y$ of minimal length with $(p,q) \in \{-1,0,1\}^2$ (see Fig. 3.2a). Compute directly $\mathbf{G}(\mathbf{R}_{ij}^{min})$ using Eq. (3.2).

- For all other $(2N_{img}+1)^2 - 1$ interactions $\{\mathbf{R}_{ij} + pL\mathbf{e}_x + qL\mathbf{e}_y \mid (p,q) \in [-N_{img}, N_{img}]^2\} \backslash \{\mathbf{R}_{ij}^{min}\}$, interpolate the corresponding far-field Green tensor at location $\mathbf{R}_{ij}^{min} \in [-L/2, L/2]^2$, using the following discrete tensor, precomputed on a grid:

$$\mathbf{G}_{mn} = \sum_{\substack{p=-N_{img} \\ p\neq 0}}^{N_{img}} \sum_{\substack{q=-N_{img} \\ q\neq 0}}^{N_{img}} \mathbf{G}\Big((-L/2 + mdx + pL)\mathbf{e}_x + (-L/2 + ndy + qL)\mathbf{e}_y\Big), \tag{3.4}$$

  with $m, n = 0, 1, ..., N_{grid} - 1$ the grid point indices and $dx = dy = L/(N_{grid} - 1)$ the grid spacing (see Fig. 3.2b). Note that the interaction due to $\mathbf{R}_{ij}^{min}$ ($p = q = 0$) is precisely *not* included in this sum.

- Sum both tensors and compute the dot product with $\boldsymbol{\sigma}_j^n$.

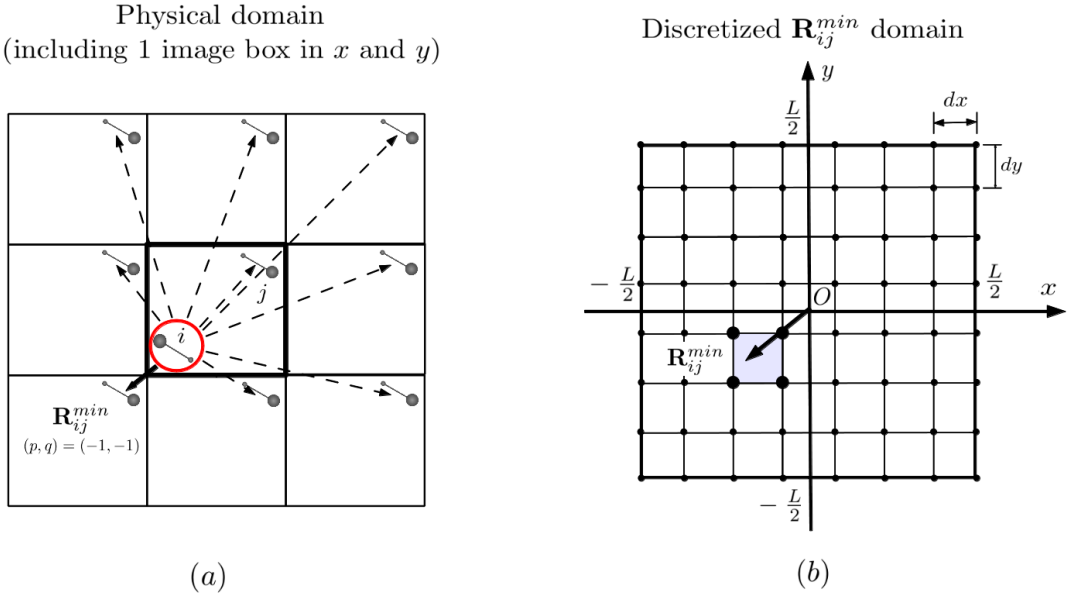

(a) (b)

FIG. 3.2: Fast computing of far-field interaction between particle i and j. (a) Compute directly the interaction with the closest particle from i (in this case, the bottom-left image $(p,q) = (-1,-1)$). (b) Approximate the Green tensor due to other particles $(p,q) \in [-N_{img}, N_{img}] \backslash \{(-1,-1)\}$: interpolate $\mathbf{G}_{mn}$ at $\mathbf{R}_{ij}^{min}$ using grid values.

The benefit of this algorithm is that the far-field Green tensor $\mathbf{G}_{mn}$ *need only be evaluated once* at the beginning of the program. At each RK4 stage and for each particle pair (i,j), the cost of summing over

$(2N_{img}+1)^2-1$ interactions is reduced to a simple bilinear interpolation, significantly enhancing the performance of the code. In a word, although the complexity of our code unfortunately remains $O(M^2)$, the implementation of this accelerated algorithm almost reduces computation time by a (constant) factor of $4[(2N_{img}+1)^2-1]$, i.e. typically 6×10^5 (for $N_{img}=200$), neglecting the one-time computation of $\mathbf{G}_{mn}$ (less than 5 min for a very fine grid $N_{grid}=250$). Note that more complex strategies to evaluate the slow-decaying Green tensor resulting from periodic images exist. To name one, the smooth particle-mesh Ewald algorithm first introduced in molecular dynamics evaluates far-field contributions using a fast-converging sum in the Fourier space and has been successfully applied to the sedimentation of fibers with a $O(M\log M)$ complexity, a significant improvement [30].

3.2 Isotropic suspensions of large-heads

3.2.1 Transition to instability and comparison with linear theory

As we saw in the previous section, our direct particle algorithm enables us to fully control the diffusion coefficients D_R and D. Similarly, the signed Péclet number $Pe=f\nu l$ and all other important dimensionless parameters introduced in the linear stability analysis of the previous chapter may be defined in particle simulations[1]. Since particles are randomly initialized in a square box of size L (diagonal length $\sqrt{2L}$), we consider that the smallest dimensionless wavenumber initially present is $k'_{min}=2\pi l/\sqrt{2}L$ (recall $l=v_s/2D_R$). The simulations that we will present next were designed for direct comparison with the linear analysis of Sec. 2.1, and more specifically, with the k'_c vs. Pe predictions of Fig. 2.1b, i.e. the threshold system size above which an homogeneous and isotropic suspension becomes unstable. For this purpose, we held f, v_s, D_R as well as the mobility parameters $\mu_\parallel=\mu_\perp=1$ and $\nu'=0$ fixed. To investigate the evolution of a given system size (or k'_{min}), L was kept constant and $\nu<0$ (hence Pe) was decreased until the first signs of collective motion[2]. As predicted by the linear analysis, instabilities were found to occur only below a certain value of Pe and individual values of ν, f, v_s, D_R did not seem to have much impact other than through the Pe ratio (for example, transition was observed roughly at the same Pe even after halving f and doubling ν). The threshold value of Pe was then associated with k'_{min}, which should actually be thought of as a critical wavenumber k'_c.

Before presenting and analyzing these results, let us discuss an issue encountered when trying to compare continous and discrete models: *the continuous notion of surface fraction is not univoquely defined in a discrete model* (see Fig. 3.3). A given $f=\sigma c_0=\sigma(M/L^2)=0.1$ ratio may be either achieved by taking a small number of large particles (Fig. 3.3a) or a larger number of smaller particles (Fig. 3.3b). Since the latter choice is closer to the continuous assumptions, we expect it to be more likely to yield comparable results. Unfortunately, a trade-off must be found due to limited computational ressources: the continuous model only remains an approximation, since simulations handle a limited number of particles. Concretely, in addition to f, one must specify which number of particles per unit area M/L^2 we use. When designing the simulations, we took $M\approx1000$ as the minimum total number

[1] We discuss in detail how to deal with the delicate case of the corrected surface fraction f in the next paragraph.

[2] The specific details of the instability and long-time behavior is treated extensively in Sec. 3.2.2.

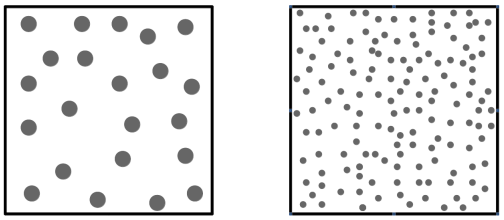

(a) (b)

FIG. 3.3: Two systems with equal $f = \sigma M/L^2$ fraction. (a) Low M/L^2 ratio: few particles with large-surface. (b) High M/L^2, closer from the continuum limit. Three M/L^2 ratios were used in simulations in order to span a variety system sizes L with constant f while keeping M in a restrictive range.

of particles to guarantee the quality of the results. On the other hand, due to the $O(M^2)$ complexity, keeping a reasonable computing time (about one day) required that we set $M \approx 6000$ as upper bound. Investigating a range of system sizes L of one order of magnitude (to cover the k_c' area of interest $[0.1, 1]$) with constant M/L^2 and σ would require to vary M over *two* orders of magnitude, in contradiction with the constraint $M \in [1000, 6000]$. We solved this issue by working with three different ratios: a coarse $M/L^2 = 450$ to investigate the $0.08 \leq k_c' \leq 0.23$ area (large boxes), $M/L^2 = 2500$ for $0.23 \leq k_c' \leq 0.53$ and a very fine $M/L^2 = 10000$ for smaller systems ($0.53 \leq k_c' \leq 1.06$). For each series of simulations, no less than six different values of k_c' were tested, always with one overlapping value to test the agreement between two consecutive ratios. The results presented in Fig. 3.4 required the analysis of dozens of simulations and enable us to compare the transition to instability with theoretical predictions.

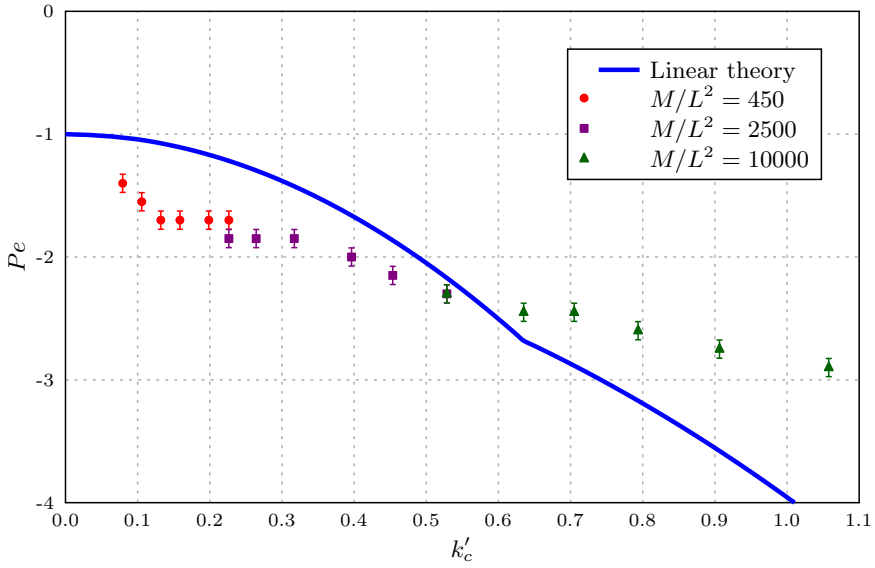

FIG. 3.4: Transition to instability of a large-head isotropic suspension ($f = \bar{H} = 0.2$, $\widetilde{H} = 0$). At a given system size (and minimal wavenumber k_c'), the threshold value of Pe below which instability occurs in particle simulations is compared with linear stability predictions. Three series of markers stand for different M/L^2 ratios needed for the whole k_c' region. Error bars indicate uncertainty due to the testing of a limited number of Pe values.

The first observation we make is that the numerical and theoretical results are of the same order of magnitude. The decreasing trend (meaning greater stability for smaller systems) is obviously confirmed, and the results even match with less than 100% of error. Note that this difference may not be explained by the uncertainty resulting from the testing of a limited number of Pe values (error bars). The agreement between both results may not seem impressive unless we recall that they result from very different approaches: on one hand a *linear* stability analysis on a *continuous* kinetic model and on the other hand a *nonlinear direct particle simulation*. In particular, let us emphasize the fact that random uniform initial conditions on a few thousand of particles *are far to induce only infinitesimal perturbations* in the first place; hence perfect agreement with the linear theory should not be expected. We further consider very encouraging the fact that (i) different "continuum approximations" (i.e. values of M/L^2) do not seem to have much influence, as shown by the results at $k_c' = 0.23$ and 0.53 (where two different M/L^2 where used) and (ii) the dimensionless group of terms $Pe = f\nu l$ seems to actually govern the instability (while in particle simulation, a given Pe may be obtained by many combinations of independent parameters).

To conclude, the simulations confirm the fact that bulk suspensions of confined large-heads are unstable above a critical system size which mainly depends upon the Péclet number. They also highlight the relevance of the kinetic model to make reasonable predictions and provide deep physical insight about the behavior of such a complex system.

3.2.2 Unstable behavior and long-time dynamics

While the previous section focused on the first signs of transition from the isotropic and homogeneous initial conditions, we now turn our attention to the specific description of the instability and long-time dynamics revealed by particle simulations.

Fig. 3.5 summarizes the main features that have been systematically observed in unstable large-head suspensions. The results presented here have been obtained using $M = 5000$ particles at a lower surface fraction than what has been used in the previous section (about 1% instead of 10%, i.e. $f = 0.02$). The box had a nondimensional size $L/l = 14$ (hence $k'_{min} = 0.317$) and we set $Pe = -2.2$ (as can be seen in Fig. 3.4, this is very near the transition which occured at $Pe \approx -1.8$). Fig. 3.5a shows *heavily polarized density waves* propagating mainly along the x direction from right to left. The time dependence is made clear by a spatiotemporal plot of the longitudinal (y-averaged) concentration (or density) field, deduced from the number of particle at a given position x (Fig. 3.5b). We see that initially small perturbations in the concentration field are amplified in a strong wave, visible from the non-dimensional time[3] $t' = tD_R = 30$ (densities reach more than twice the average system density). A spatiotemporal diagram of the global orientation $\theta = \cos^{-1}(\mathbf{p} \cdot \mathbf{e}_x)$ (Fig. 3.5c) further shows that the polarization of the growing wave starts roughly at the same time: here $\theta \approx -\pi$ rapidly becomes the preferred orientation in the system, explaining the wave propagation in the $-x$ direction. The growth of the global polarization is more qualitatively measured in Fig. 3.5d, where we see that $P = |\langle \mathbf{p} \rangle| = \sqrt{\langle p_x \rangle^2 + \langle p_y \rangle^2}$ increases dramatically after $t' = 30$ (here $\langle \cdot \rangle$ denotes the average all particles $1/M \sum_{i=1}^{M}$). This figure also features

[3] As we focus here on stability, we non-dimensionalize the time the same way as we did for the growth rate $\alpha' = \alpha/D_R$.

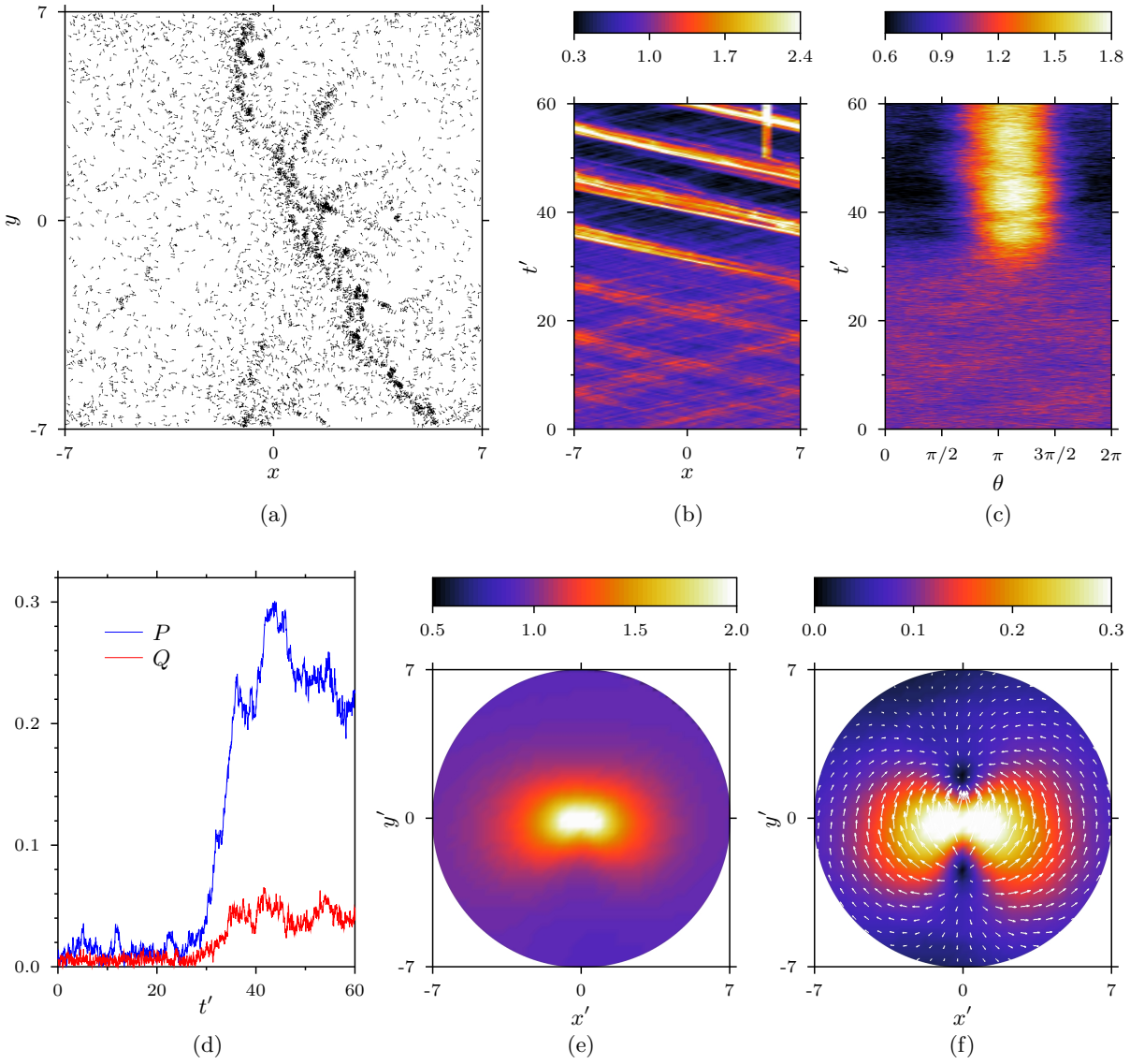

FIG. 3.5: Nonlinear dynamics of $M = 5000$ initially isotropic large-head swimmers for $Pe = -2.2$, $f = 0.02$, and $k'_{min} = 0.317$ ($L/l = 14$). (a) Snapshot of the particles at $t' = tD_R = 42.7$ showing the polarized density waves. (b) Spatiotemporal diagram of the longitudinal concentration and (c) global orientation distribution (1 is system average). (d) Norm of polarization P and nematic order Q. (e) Pair distribution function for the concentration (1 is system average) and (f) the polarization (norm and direction) averaged between $t' = 35$ and 55.

the nematic order parameter Q, or positive eigenvalue of the average nematic tensor $\langle \mathbf{Q} \rangle = \langle \mathbf{pp} - \mathbf{I}/2 \rangle$ (note that $0 \leq Q \leq 1/2$). The growth of this parameter reveals that waves tend to adopt a slight *splay* shape (recall Fig. 1.4b), as could be qualitatively anticipated from the typical curvature observed in Fig. 3.5a. Note that this instability characterized by travelling fluctuations in concentration, polarization and, to a lesser extent, splay in medium-sized systems (slightly below the Pe transition) *agrees remarkably well with the predictions of the linear stability analysis* (see Sec. 2.3.4). The next two plots represent *pair*

distribution functions of the concentration (Fig. 3.5e) and polarization (Fig. 3.5f). They are computed by considering a particle i and switching to its frame of reference such that the origin $(x', y') = (0, 0)$ lies at $\mathbf{R}_i$. We then search over all $j \neq i$ particles and assign to (x', y') a value proportional to the number of particles lying around this point (1 is the average). Similarly, the pair polarization at (x', y') results from the projection of all $\mathbf{p}_j$ of particles lying near (x', y') on the reference $\mathbf{p}_i$. This whole procedure is repeated in order to average over every particle i and give a meaningful picture of the correlations in the system. The high pair concentration in a horizontal band observed in Fig. 3.5e (up to twice the system mean value) means that most particles have many neighbors at their left and right side, while their front and back region is depleted, in consistency with the notion of waves that emerged from previous representations. Furthermore, the rather high norm (up to 0.3) of the pair polarization in the same band (Fig. 3.5f) confirms the strong correlation of the particle orientations inside a wave. The direction of the pair polarization (see the white arrows) further suggests that particles behind the wave tend to align (and therefore swim) *away from the wave*, whereas particles located in front of the wave tend to *swim against it*, which is bound to give rise to collisions.

In essence, polarization waves behave like a giant dipole (see the clear dipole pattern of the pair polarization) attracting particles with opposite swimming direction at their front. This crucial observation enables us to understand the formation of high density *balls*, visible in the spatiotemporal concentration diagram Fig. 3.5b. We indeed notice from $t' \approx 50$ a highly concentrated region (at $x \approx 5$) which, after closer examination, may be shown to consist in a stable axisymmetric structure where particles lie on a circle of finite radius, swimming toward the center and each particle being kept at constant location by the repulsive flow of others. Fig. 3.6a shows the spatiotemporal concentration diagram of a similar

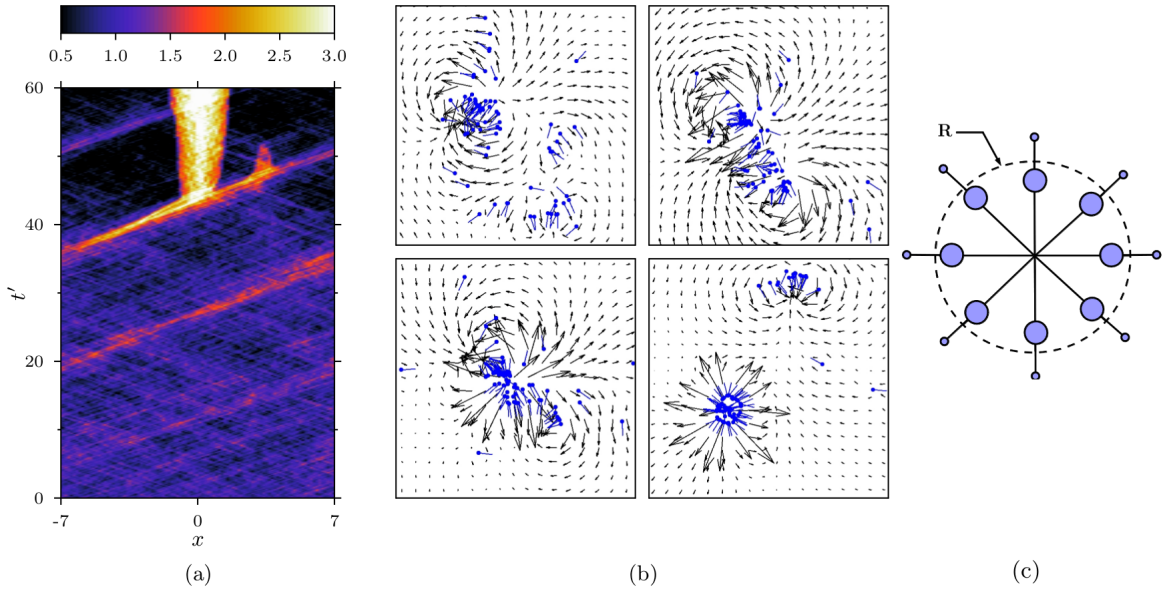

FIG. 3.6: (a) Spatiotemporal concentration for similar parameters used in Fig. 3.5, except $M = 2500$ and $f = 0.2$ showing the rapid formation of a large high-density "ball" from a polarized wave. (b) Snapshots of particles and velocity field illustrating the formation of such balls (c) Analytical model for the steady radius of such clusters.

simulation, where the concentration has been increased by a factor of 10 (mean surface fraction is now 10%). We see that such balls can reach dramatic dimensions in that case, attracting most of the system's particles and destroying any propagating wave within a few seconds. We provide more details about the early stages of the formation of such structures in Fig. 3.6b, where a few particles experiencing the phenomenon of interest are plotted together with the flow they generate. First, particles with strongly correlated orientation emerging from the instability described above (polarized density wave) behave like a giant dipole, repelling particles at their tail and attracting them at the front (the apparent paradox comes from the fact that large-heads align, and thus swim, *against* the flow). After many particles with opposite orientation have joined the first wave, a circular structure rapidly emerges for reasons of greater stability. A steady radius is attained, and the resulting ball generates a high positive diverging flow, attracting all the surrounding particles towards its center, explaining the inescapable growth of such a pattern. We now understand why the initially small ball of Fig. 3.5b strenghtens as it is being hit by the main polarized wave at $t' = 55$.

To provide more insight into the intuitive fact that systems of higher concentration form higher balls, we analytically derived the steady state radius R of a single layer of particles evenly spaced around a circle (see Fig. 3.6c). The calculations detailed in Appendix A yielded the surprisingly simple closed-form solution $R = \sqrt{\sigma(M^2-1)/24\pi}$, which may very well be approximated by $R \approx 0.115\sqrt{\sigma}M$, that is such balls increase linearly in size with both the number of particles and their size ($\sim \sqrt{\sigma}$). Numerical simulations initializing particles on a circle of arbitrary radius confirmed the value of the equilibrium radius and a simple analysis further suggested that the stability of such a circular structure increases linearly with M. Note however that considering disk-shaped particles of area 2σ, the sum of the diameters of particles $M\sqrt{2\sigma/\pi} \approx 0.80\sqrt{\sigma}M$ always exceeds the perimeter of the circle $2\pi \times 0.115\sqrt{\sigma}M \approx 0.72\sqrt{\sigma}M$ by about 10%, causing overlapping. Unfortunately, the model we use for interactions based on the dilute limit does not hold in that case and taking into account contacts would prevent R to take such a small value. We nonetheless believe that the main conclusions of this analytical and numerical investigation give valuable basis to explain that very dilute suspensions are prone to the formation of smaller, less stable balls having less influence over the whole system which keeps exhibiting the original polarized density wave pattern over relatively long times (as in Fig. 3.5). By contrast, since the balls in systems of larger particles are larger in the first place, the diverging flow they create is felt in a larger fraction of the system, explaining their faster growth and the emergence of quasi-stable multi-layered structures (as in Fig. 3.6a). Let us emphasize again that the model upon which our theory and simulations rely *does not apply out of the dilute limit* which explains why results in which such high-density areas become dominant are highly questionable.

3.3 Isotropic suspensions of large-tails

In the previous section, we detailed the transition to instability and long-time dynamics observed in large-head suspensions, and concluded that numerical results are strongly supported by the linear theory. In this section, we show that although isotropic suspensions of large-tails have been proved to be linearly

stable (see Sec. 2.3.4), simulations demonstrate that nonlinearities may quickly drive such a system away from the base state and trigger fascinating large-scale dynamics.

Motivated by the relevance of the stability transition predictions for the $Pe < -1$ instability (see Fig. 3.4), we start by a very similar thorough study of the Pe value for which a system characterized by k_c' shows the first signs of collective motion. The idea is to see whether or not large-tails are also prone to long-wavelength instability (i.e. the growth rate increases with smaller k'). The results presented

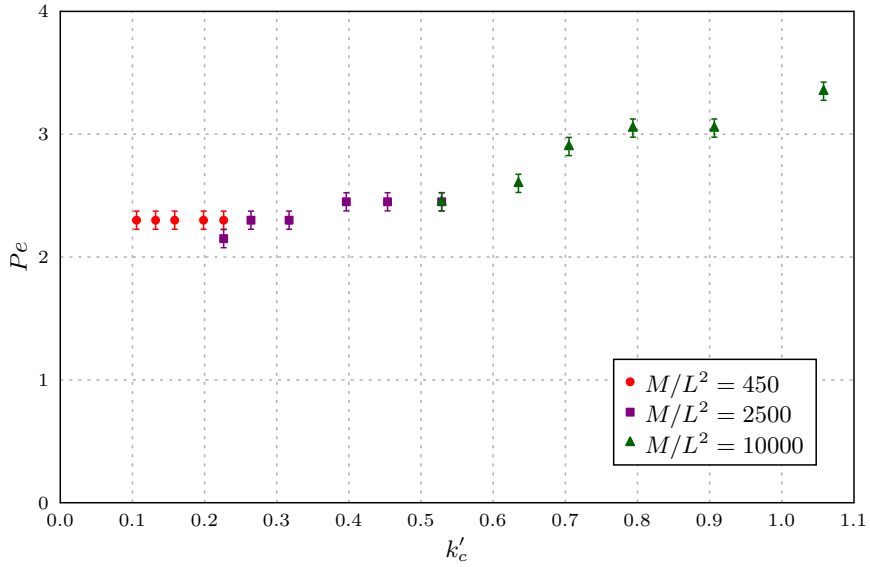

FIG. 3.7: Transition to instability of large-tail suspensions ($f = 0.2$). For a given system size and critical wavenumber k_c', collective motion is found only above a certain Pe. Error bars and M/L^2 ratios are as in Fig. 3.4.

in Fig. 3.7 indeed confirm our conjectures: this large-tail nonlinear instability shares these very special characteristics with the large-head one. The transition Pe value indeed increases with k_c', meaning that instability is found only above a critical system size. We also note that for the range of system sizes considered, the Pe values are of the same order of magnitude (in absolute value) than the ones causing large-head collective motion. Recalling the physical arguments and the meaning of Pe as a self-advection/diffusion ratio, this provides evidence for the idea that both instability mechanisms ultimately stem from the combination of dipolar interactions and polar shape of particles.

We now turn to the specific description of the dynamics observed in particle simulations. The results of Fig. 3.8 were obtained for $M = 3600$ particles in a box of size $L/l = 17$ ($k_c' = 0.26$) with a mean area fraction of 10%. The Péclet number used here ($Pe = 3.7$) is slightly above the transition (in this case, $Pe \approx 2.2$, see Fig. 3.7). As shown in Fig. 3.8a, such systems typically form *two counter-rotating vortices*. This observation is more quantitatively supported by Fig. 3.8f and Fig. 3.8g, showing respectively the pair concentration and polarization introduced previously. We see that particles are much more likely to have neighbors swimming at their front and back (with which they have strongly correlated orientation) than at their sides (where little correlation is found). As in the previous section, the spatiotemporal longitudinal

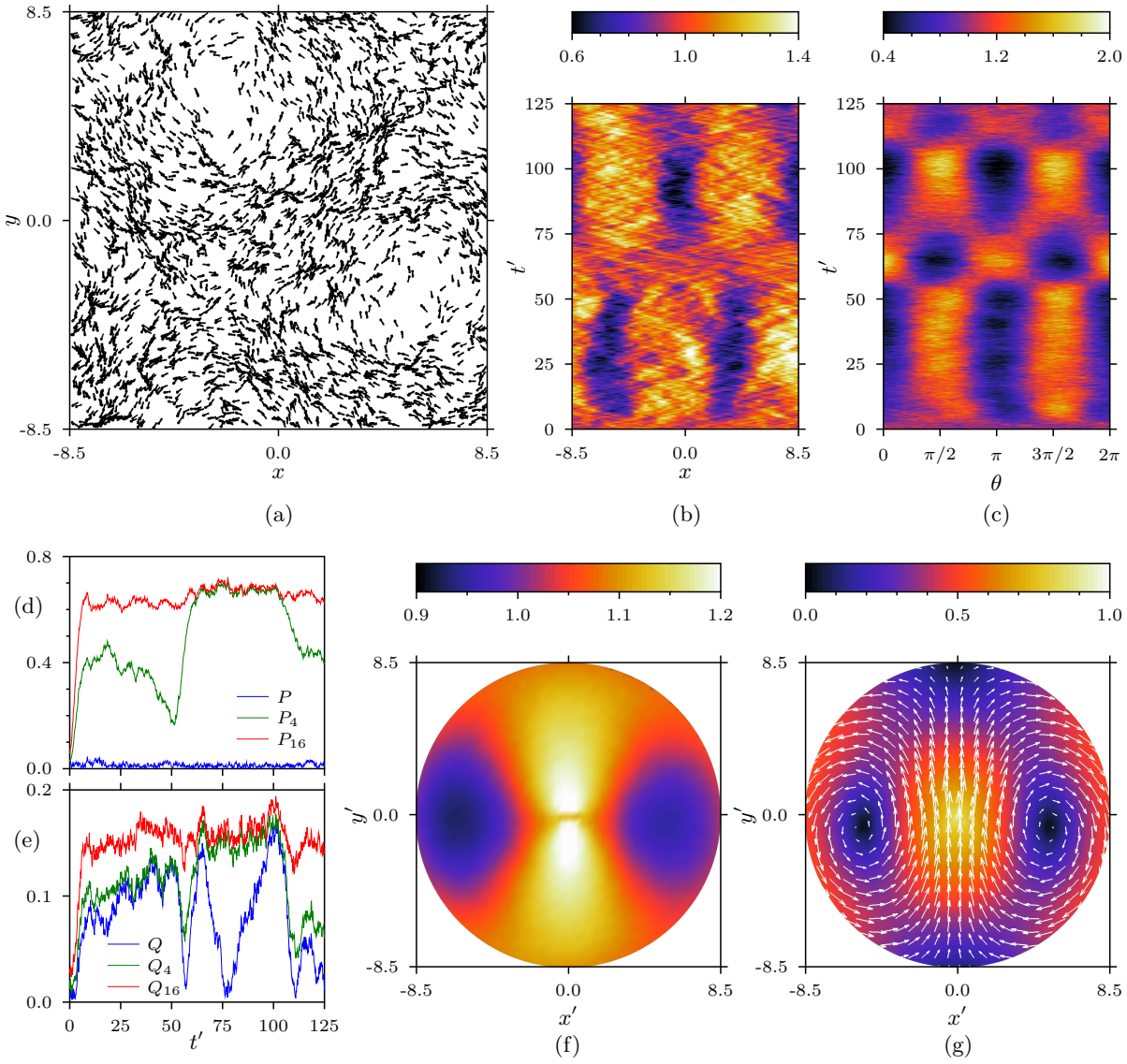

FIG. 3.8: Nonlinear dynamics of $M = 3600$ initially isotropic large-tail swimmers for $Pe = 3.7$, $\sigma c_0 = \bar{H} = 0.2$, $\widetilde{H} = 0$ and $k'_{min} = 0.26$ ($L/l = 17$). (a) Snapshot of two counter-rotating vortices at $t' = 92$. (b) Spatio-temporal plot of the longitudinal concentration field and (c) the global orientation distribution showing the quasi-periodic formation and break-up of patterns. (d) Global and local polar and (e) nematic order. (f) Pair distribution function for the concentration and (g) the polarization (norm and direction) averaged over the last 7 time units.

concentration (Fig. 3.8b) and orientation (Fig. 3.8c) uncover the time dependence of this interesting dynamics and reveal that the system essentially *behaves in a quasi-periodic fashion*. Specifically, we observe alternance between two kinds of steady vortices: (*i*) one with clear concentration fluctuations in x (corresponding the the circular depleted regions) and a preferred direction $\theta \approx \pm\pi/2$ (see for instance the snapshot Fig. 3.8a at $t' = 92$) and (*ii*) another with rather vertical concentration patterns (not represented here) and a preferred direction $\theta \approx \pm\pi$. More insight into the quasi-periodic formation of

vertical and horizontal vortices may be gained by studying the time evolution of the polar and nematic order parameters (Fig. 3.8d and Fig. 3.8e respectively). In addition to the norm of the global polarization P and the positive eigenvalue of the nematic tensor Q introduced previously, we focus here on *local* parameters P_K, Q_K, where the averaging process is first made within K smaller boxes of linear size $L/\sqrt{K}$: $P_K = 1/K \sum_{k=1}^{K} |\langle \mathbf{p} \rangle_k|$, where $\langle \cdot \rangle_k$ denotes the average over the particles located inside the k-th box (Q_K is obtained in a similar way). Unlike the *global* polarization $P = 0$, we see that P_4, P_{16} reach very high values during the vortex structures, confirming the fact that particles are *locally* heavily polarized. The values of the nematic parameters further prove that the particles exhibit splay and bend alignment at all scales, as expected by the observed pattern. Eventually, the dramatic decrease of P_4 and Q observed during the change between the two vortex structures is interpreted as the consequence of the *break-down of large-scale structures* (of lengthscale $L/2$ for the polarization and L for the nematic alignment, in consistency with the counter-rotating vortex structure). During these transition phases, the values of P_{16}, Q_4, Q_{16} prove that smaller-scales structures with relatively high orientational or nematic order are however still present (of lengthscale $L/4$ for P and $L/2$ for Q).

3.4 Density waves in a narrow channel with external flow

In Sec. 2.2 we showed that spatially uniform suspensions subject to a constant external flow $\mathbf{U}_0 = U_0 \mathbf{e}_x$ adopt a polar stationnary state $\Psi(\mathbf{x}, \mathbf{p}) = c_0 \Psi_0(\theta)$, where $\theta = \cos^{-1}(\mathbf{p} \cdot \mathbf{e}_x)$ and $\Psi_0(\theta)$ depends on the nondimensional flow strength $\xi = \nu U_0 / D_R$ (see Eq. (2.31)). We demonstrated that large-heads were in general significantly stabilized by this flow, and based on our last conclusions, we may assume a similar consequence for large-tails. This motivates the study of the dynamics of such quasi-aligned active suspensions in a narrow channel. Keeping in mind recent results reporting 1D Burgers density waves in droplet ensembles advected in a 1D channel [17, 18, 19], this section seeks to investigate the quasi-one-dimensional (q1D) density behavior of polar, active suspensions in a narrow channel of length L, rigidly bounded in y with width $W \ll L$.

3.4.1 Quasi-one-dimensional continuum model

To start with, insight may be gained by deriving a q1D model based on the continuous kinetic model and mean-field description used throughout this work. For this purpose, we make the following self-consistent set of assumptions:

- constant, uniform external flow along x: $U_0 \mathbf{e}_x$, and a polar, stable base state for the orientation distribution: $\Psi_0(\theta) = A \exp(\xi \cos\theta)$, with A such that $\int_0^{2\pi} \Psi_0(\theta)\, \mathrm{d}\theta = 1$,

- one-dimensionality: we assume a sufficiently narrow channel such that transversal effects and variations may be neglected: $\Psi(x, y, \theta, t) = c(x, t)\Psi_0(\theta)$ and $\mathbf{u}(x, y, t) = u(x, t)\mathbf{e}_x$,

- confinement in y is not strong enough to significantly change the nature of the interactions: $W \gg a$. This avoids us the tedious analytical treatement of the influence of boundaries.

We now aim at deriving a 1D evolution equation for the concentration field $c(x,t)$. Since anisotropy itself does not play any relevant role here, we set $\mu_\perp = \mu_\parallel = 1$ and $\nu' = 0$. Integrating the continuity equation Eq. (1.7) with respect to θ and plugging in our ansätze yields

$$\frac{\partial c}{\partial t} = -\frac{\partial}{\partial x}(v_s P_0 c + cu) + D\frac{\partial^2 c}{\partial x^2}. \tag{3.5}$$

where $0 < P_0 < 1$ is the norm of the polarization given by Eq. (2.32). To decouple the velocity from Eq. (3.5) we use the divergence of the velocity Eq. (2.6) together with the dipolar solution Eq. (1.3) (assumed valid despite the confinement in y) and it follows that

$$\frac{\partial u}{\partial x} = -\sigma v_s P_0 \frac{\partial c}{\partial x} \qquad \text{and} \qquad u = -\sigma v_s P_0 c + U_0. \tag{3.6}$$

Combining Eqs. (3.5), (3.6) yields the following conservation law:

$$\frac{\partial c}{\partial t} + \Big(U_0 + v_s P_0(1 - 2\sigma c)\Big)\frac{\partial c}{\partial x} = D\frac{\partial^2 c}{\partial x^2}. \tag{3.7}$$

We can alternatively write Eq. (3.7) in conservative form

$$\frac{\partial c}{\partial t} + \frac{\partial q}{\partial x} = D\frac{\partial^2 c}{\partial x^2} \qquad \text{with the flux} \qquad q = \Big(U_0 + v_s P_0(1 - \sigma c)\Big)c. \tag{3.8}$$

This first-order, hyperbolic, quasilinear equation is commonly used as a simple 1D model for *traffic flow behavior* [31]. The prefactor $v_s P_0(1 - \sigma c)$ in the flux must be interpreted as an Eulerian *concentration dependent velocity*. The single-swimmer Lagrangian effective velocity $v_s P_0$ along x is renormalized by interactions: it is maximal where $c(x) = 0$ and *decays* linearly with c to reach 0 where $c(x) = 1/\sigma$ (the maximal concentration). Wave solutions of this equation are characterized by the emergence of *a shock at the tail* and *a rarefaction wave at the front*. The aerial view of a typical traffic jam gives an intuitive and familiar illustration of both phenomena. These many-body systems of strongly interacting vehicles prone to pattern formation indeed share similarities with active fluids. Their complex physical behavior has been studied by various nonlinear wave equations, including Eq. (3.7), which remains the simplest model accounting for density waves (for a review see [32]).

To conclude, our q1D kinetic model predicts density waves which strongly contrast with the ones previously observed in driven droplets colonies, characterized by *increasing* velocity with local concentration [17, 19] and explained by the influence of boundaries in y, which we precisely neglected here. The new and opposite behavior we predict indeed genuinely arises from self-propulsion (v_s is in factor of $(1 - \sigma c)$ in q), which explains why it has not been previously observed in confined but passive droplet colonies.

3.4.2 Comparison with particle simulations

We shall now see if the predicted behavior is actually confirmed by particle simulations. To carry out simulations in this new geometry, we decided to take into account the influence of the boundaries on interactions, neglected by necessity in the q1D continuum model but which give rise to radically different density waves in the passive case. Whereas the no-slip boundary condition at $y = \pm W/2$ cannot be satisfied (the velocity is assumed to be potential), non-penetration must certainly hold and its enforcement

required a new system of images and modifications in the accelerated algorithm that we describe in Appendix B.

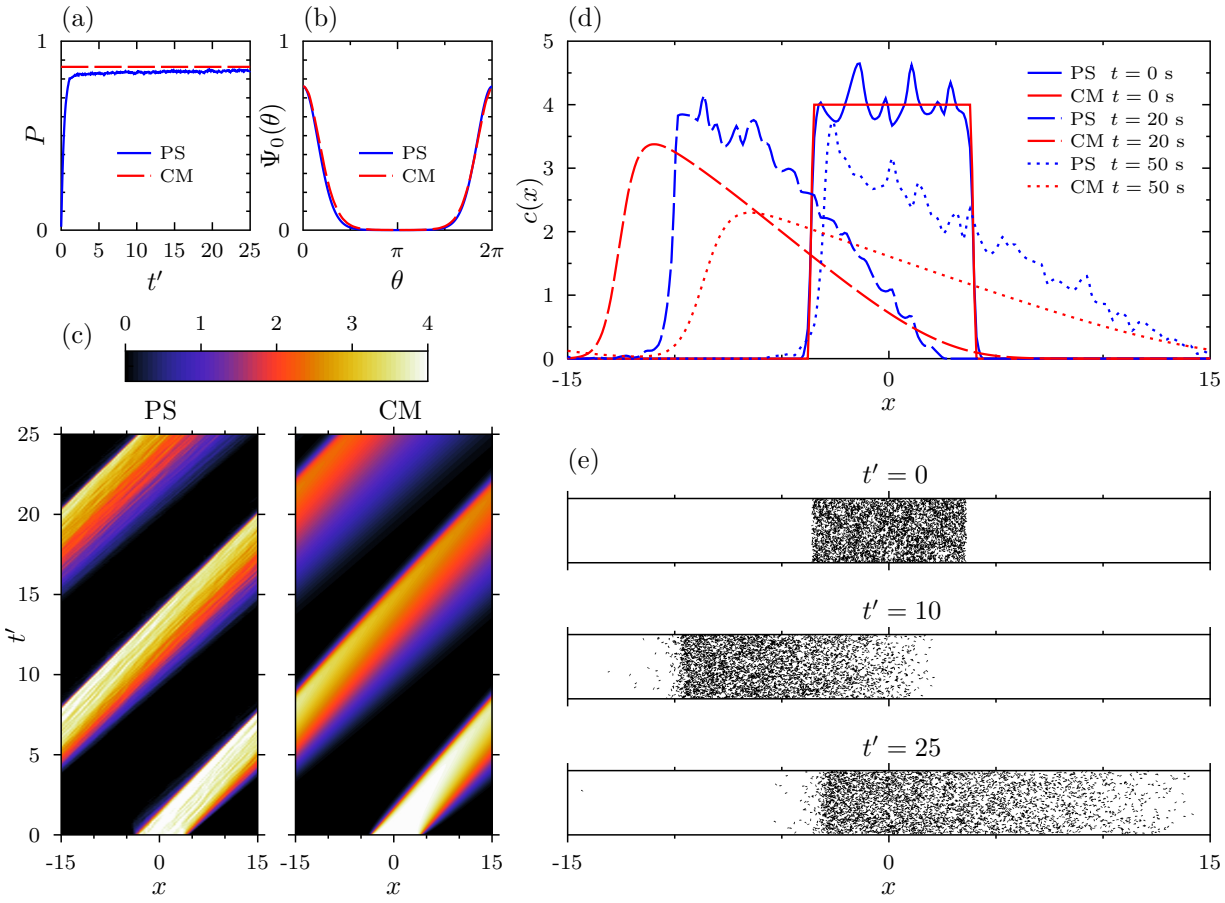

FIG. 3.9: Density waves in a narrow channel with external flow. Comparison of particle simulation (PS) ($M = 4000$ particles, $\sigma c_0 = 0.1$, $\xi = +4$, $L/l = 30$, $W/l = 3$) and FD solution of Eq. (3.8) (continuum model, CM). (a) Polarization P rapidly reaching P_0 (polar stable state). (b) Orientation distributions (PS is averaged over $t' = tD_R \in [5, 25]$ interval). (c) Spatiotemporal y-averaged concentrations showing rarefaction wave at the front and shock at the tail. For clarity, normalization is made such that the average concentration is 1. (d) Concentration profiles at selected times, and (e) corresponding PS snapshots (particles are magnified).

The theoretical predictions have been tested using $M = 4000$ large-tail particles in a channel of aspect ratio $L/W = 10$. Particles are initially isotropic and concentrated in a narrow band $x \in [-L/8, L/8]$, simulating the initial state of a prototypical traffic jam (an average surface fraction of 5% has been chosen so that even the initial state may be considered dilute). The strength of the external flow used $\xi = 4$ enabled very fast convergence of this initially isotropic system to the stable polar state, as shown in Fig. 3.9a (P quickly reaches P_0) and Fig. 3.9b (for $\Psi_0(\theta)$), allowing for direct comparison with the conservation law derived above. Fig. 3.9c and Fig. 3.9d indeed show the time evolution of the longitudinal (y-averaged) concentration profile $c(x, t)$ obtained in the particle simulation (PS) and in the continuum

model (CM), by a reference finite-difference solution of Eq. (3.8).

The striking traffic flow behavior observed in simulations characterized by rarefaction at the front and shock at the tail (see also the snapshots in Fig. 3.9e) agrees very well with the results of the continuum model, which neglected the influence of confinement on interactions. This demonstrates that, at least in these conditions of weak confinement (aspect ratio of the domain is 10 and $W \gg a$), *the effects of self-propulsion on the global traffic flow dynamics significantly overweigh the influence of the channel boundaries*, which might only be perceptible in passive suspensions. Interestingly, the observed behavior does not seem to depend much upon the rather perturbed initial concentration profile resulting from random initialization of particles (see Fig. 3.9d), confering a relative generality to this result. We however note that the density wave tends to propagate with higher phase speed and lower diffusion than expected by the q1D model. In particular, the steep gradient at the tail seems much less aftected by diffusion than the rest of the wave.

One possible explanation for the higher phase speed might be the role of boundaries, possibly through a similar mechanism that resulted in a positive local coupling of velocity and concentration in the case of driven droplets (see [17] for details). The fact that this coupling is precisely *not* observed here indicates that this conjecture needs a more thorough analysis. We would like to conclude this section with a more satisfactory, although purely qualitative, explanation for the space-dependent diffusion observed. Recall from Sec. 1.4 that the $D = v_s^2/2D_R$ approximation was obtained by neglecting diffusion due to hydrodynamic interactions and assuming an elementary isotropic diffusion mechanism. The superposition of a external flow along x resulting in polar alignment clearly breaks isotropy and makes translational diffusion much more likely to occurs *in the direction of the flow*, where particles have a net self-propulsion velocity $v_s P_0$, explaining the low $-x$ diffusion at the tail and the lasting steep gradient. We are very confident in the fact that improvements of the q1D diffusion model may account more quantitatively for this phenomena.

Conclusions and directions for future work

In this work, we have considered various problems in which collective dynamics and pattern formation spontaneously arise in suspensions of swimming organisms as a consequence of individual hydrodynamic interactions. Motivated by the complex behavior reported in unbounded bulk suspensions, we focused on the influence of rigid confining boundaries, known to change the nature of interactions and for which little is known. The approach followed has consisted in investigating a few systems of biological relevance, by means of theory and numerical discrete particle simulation.

In Chapter 2, we have used a mean-field continuum kinetic model based on a conservation equation for the probability distribution of particle positions and orientations, coupled to the Stokes equations for the fluid flow, with a modified incompressibility term arising from the relative velocity of swimmers with the background flow. We first performed a linear analysis of the stability of an isotropic confined suspension, the most relevant problem in the context of thin microbial colonies and other biologically active films. We confirmed the previous result that large-head organisms are subject to a long-wavelength generic instability, and our analysis provided the first detailed description of the resulting large-scale dynamics and wavenumber dependence. We demonstrated that systems larger than a threshold size were subject to propagating polarized density waves and discussed the influence of a number of parameters on the transition criterion. We then extended this analysis to investigate the influence of a constant external flow, which has been found to stabilize large-heads by controlling their orientation. We finally addressed the linear stability of a suspension of aligned swimmers and explained that colonies of both large-heads and large-tail experience short-wavelength instabilities. We concluded that local alignment cannot even be reached at the smallest scale of the system, meaning that this base state had no practical relevance.

In Chapter 3, we used an efficient direct particle simulation algorithm to simulate the long-time dynamics of confined isotropic suspensions of thousands of swimmers. Simulations of large-heads successfully captured the polarized density waves predicted by our linear theory and we found good agreement with the stability criterion on the system size. We then discovered that apart from very dilute systems, this instability is typically followed by the formation of very dense, stable circular structures with converging particles. Combining long-time nonlinear numerical results, an analytical solution for the equilibrium shape of these clusters and insightful physical arguments, we elucidated the mechanisms behind the

emergence and growth of these interesting patterns. We then investigated the nonlinear dynamics of large-tails colonies and revealed a similar long-wavelength instability that had not been predicted by the linear analysis. We captured the salient features of this complex and fascinating dynamics including the quasi-periodic formation and break-down of large-scale counter-rotating vortices. Finally, motivated by our linear results, we shed light on the dynamics of swimmers subject to a stabilizing external flow in a narrow channel, a situation of practical relevance enabling simple analytical treatment. Using a quasi-one-dimensional kinetic model, we demonstrated that individual self-propulsion was significantly rescaled by interactions, resulting in a nonlinear traffic flow equation for the Eulerian particle density owing to the local coupling between velocity and concentration. Simulations confirmed the predicted shock formation and rarefaction wave in a typical traffic jam problem.

Although this work has focused on a few model problems, we believe that the physical mechanisms we identified have broader implications for various phenomena in the fields of complex fluids, soft-matter and many-body physics. As demonstrated throughout this work, confined active suspensions exhibit rich dynamics while being exceptionnally well-suited for analytical and computational investigation. The linearity of the flow equations and the low dimensionality of the system indeed enabled extensive theoretical treatment and the relative fast decay of the interactions with respect to the system dimensionality allowed for the direct numerical simulation of large systems at no cost using very simple algorithms. For these reasons, we are convinced that further study of confined living fluids could pave the way for a better understanding of how the coupling of a large number of degrees of freedom by long-ranged interactions translates into complex dynamics and pattern formation. In this respect, and since progress in understanding the dynamics of swimming microorganisms is also of paramount interest in biological, ecological, industrial or medical applications, we shall give a few directions to extend this work in the hope of describing more faithfully some phenomena observed in experiments.

First, further efforts to elucidate the interesting traffic flow behavior of swimming organisms in very narrow channels could concentrate on the influence of boundaries on interactions. In addition, improvements in its theoretical description could also include anisotropic diffusion, which takes place when the symmetry is broken by an imposed flow. More generally, all the problems we tackled in this work involved dilute suspensions, and although our simple models based on the mean- and far-field description of hydrodynamic interactions were sufficient to capture interesting behavior, we shall emphasize that the modeling of more concentrated suspensions probably remains the greatest challenge. In the case of initially dilute large-heads, we showed for example that long-time dynamics was characterized by the formation of much higher-density structures, poorly described by our model. To avoid the overlapping of particles in our simulations, we attempted to include a hard-sphere contact algorithm, which resulted in the absence of any collective motion, certainly because of the too basic ad-hoc treatment of the particle orientations during collisions. Furthermore, numerical evidence suggests that steric interactions alone can give rise to coherent structures [33]. Motivated by a recent successful attempt in 3D [13], extending our model to include steric interactions or near-field hydrodynamic effects could enable us to critically assess the relative roles of hydrodynamic vs steric interactions.

Appendix A

Steady state of swimming particles distributed around a circle

In this appendix, we investigate the case of a collection of N particles, uniformly distributed at locations $\mathbf{R}_i$, $i = 1, ..., N$ around a circle centered at the origin and oriented toward the center $\mathbf{p}_i = -\mathbf{R}_i/|\mathbf{R}_i|$, as sketched on Fig. A.1. The objective is to derive the steady state radius R of the circle.

We start by using the equation of motion for the position of a self-propelled particle in confined geometries Eq. (1.4a), since the steadiness of the orientations $\mathbf{p}_i$ is automatically satisfied given te geometry of the problem. Assuming that $\mu_\perp = \mu_\parallel = 1$ for simplicity, Eq. (1.4a) reduces to

$$\dot{\mathbf{R}}_i = v_s \mathbf{p}_i + \sum_{\substack{j=1 \\ j\neq i}}^{N} \mathbf{u}^d(\mathbf{R}_i|\mathbf{R}_j, \boldsymbol{\sigma}_j) = 0 \quad \text{for all} \quad i = 1, ..., N, \tag{A.1}$$

with $\boldsymbol{\sigma}_j = \sigma[\dot{\mathbf{R}}_j - \mathbf{u}(\mathbf{R}_j)] = \sigma v_s \mathbf{p}_j$. As sketched in Fig. A.1, the symmetry of the problem makes all particles equivalent, such that we can focus on any arbitrary particle, for example $i = N$. Eq. (A.1) therefore reduces to a single vector equation for $\dot{\mathbf{R}}_N$, which, recalling Eq. (1.3), takes the form

$$\sum_{j=1}^{N-1} \frac{1}{2\pi|\mathbf{R}_{Nj}|^2}(2\hat{\mathbf{R}}_{Nj}\hat{\mathbf{R}}_{Nj} - \mathbf{I}) \cdot \mathbf{p}_j = -\frac{1}{\sigma}\mathbf{p}_N, \tag{A.2}$$

where $\mathbf{R}_{Nj} = \mathbf{R}_N - \mathbf{R}_j$ and $\hat{\mathbf{R}}_{Nj} = \mathbf{R}_{Nj}/|\mathbf{R}_{Nj}|$. Assuming that $\mathbf{p}_N = \mathbf{e}_y$ as in Fig. A.1, and by symmetry of the dipolar flows, all x components cancel out and Eq. (A.2) reduces to a single algebraic equation. Let us now distinguish between two cases, depending on whether the number of particles is odd $N = 2n - 1$ or even $N = 2n$. Based on previous symmetry considerations, the odd case requires a sum over $n - 1$ particles (see the blue particles on the right half of the circle $i = 1, 2$ in Fig. A.1), whereas the even case must include the additionnal contribution of particle n (see the green particle $i = 3$), whose specificity is to lie exactly at the opposite of particle N (the red particle). We are therefore able to formally restate

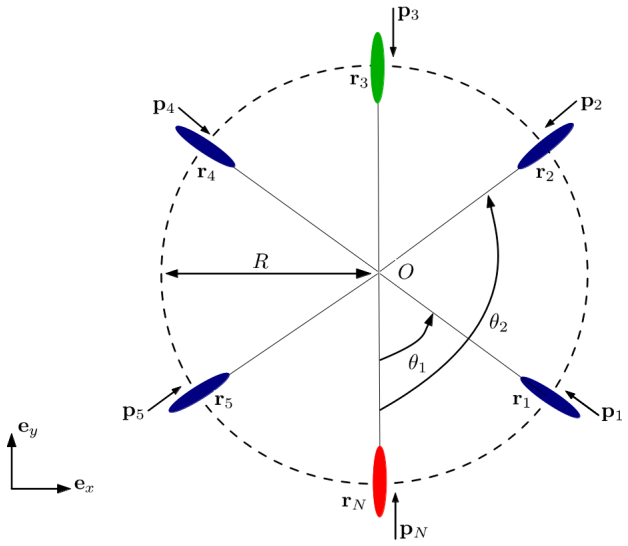

FIG. A.1: $N = 6$ particles evenly spaced around a circle and swimming toward its center O. The equilibrium radius R is computed by summing the interactions of the blue (if N is odd) or blue and green (if N is even) particles at the red particle's location and cancelling its velocity $\dot{\mathbf{R}}_N$

Eq. (A.2) as

$$\underbrace{2\sum_{j=1}^{n-1}\frac{1}{2\pi|\mathbf{R}_{Nj}|^2}(2\hat{\mathbf{R}}_{Nj}\hat{\mathbf{R}}_{Nj}-\mathbf{I})\cdot\mathbf{p}_j\cdot\mathbf{e}_y}_{1}=-\frac{1}{\sigma}\quad\text{if } N=2n-1, \tag{A.3}$$

$$\underbrace{2\sum_{j=1}^{n-1}\frac{1}{2\pi|\mathbf{R}_{Nj}|^2}(2\hat{\mathbf{R}}_{Nj}\hat{\mathbf{R}}_{Nj}-\mathbf{I})\cdot\mathbf{p}_j\cdot\mathbf{e}_y}_{1}+\underbrace{\frac{1}{2\pi|\mathbf{R}_{Nn}|^2}(2\hat{\mathbf{R}}_{Nn}\hat{\mathbf{R}}_{Nn}-\mathbf{I})\cdot\mathbf{p}_n\cdot\mathbf{e}_y}_{2}=-\frac{1}{\sigma}\quad\text{if } N=2n. \tag{A.4}$$

Using the angles $\theta_j = 2\pi j/N$ sketched in Fig. A.1, it straightforward to show that $\mathbf{R}_{Nj} = -R\,(\sin\theta_j, 1-\cos\theta_j)$ and $\mathbf{p}_j = -(\sin\theta_j, \cos\theta_j)$. Basic trigonometric and matrix manipulations yield

$$\frac{1}{2\pi|\mathbf{R}_{Nj}|^2}(2\hat{\mathbf{R}}_{Nj}\hat{\mathbf{R}}_{Nj}-\mathbf{I})\cdot\mathbf{p}_j\cdot\mathbf{e}_y=\frac{-1}{4\pi R^2(1-\cos\theta_j)}, \tag{A.5}$$

for any $j = 1, ..., N-1$. This will be used for $j = 1, ..., n-1$ (term 1) and note that in the particular case $j = n$ (term 2) it reduces to $-1/8\pi R^2$. It follows that Eqs. (A.3), (A.4) simplify to

$$\sum_{j=1}^{n-1}\frac{1}{1-\cos\theta_j} = \frac{2\pi R^2}{\sigma}\qquad\text{if } N=2n-1, \tag{A.6}$$

$$\sum_{j=1}^{n-1}\frac{1}{1-\cos\theta_j}+\frac{1}{4} = \frac{2\pi R^2}{\sigma}\qquad\text{if } N=2n. \tag{A.7}$$

Solving Eqs. (A.6), (A.7) requires that we evaluate the following sums, respectively

$$S_n^1=\sum_{j=1}^{n-1}\frac{1}{1-\cos\left(\frac{2\pi j}{2n-1}\right)}\qquad\text{and}\qquad S_n^2=\sum_{j=1}^{n-1}\frac{1}{1-\cos\left(\frac{\pi j}{n}\right)}, \tag{A.8}$$

Computing the first few terms enabled us to guess empirically the general form of each sum, which is surprisingly simple. It could then be proved using mathematical induction that

$$S_n^1 = \frac{1}{3}(n^2 - n) = \frac{1}{12}(N^2 - 1) \qquad \text{and} \qquad S_n^2 = \frac{1}{3}(n^2 - 1) = \frac{1}{12}(N^2 - 1) - \frac{1}{4}, \tag{A.9}$$

recalling the fact that $N = 2n - 1$ for S_n^1 and $N = 2n$ for S_n^2. Eventually, Eqs. (A.6), (A.7) both reduce to the exact same equation[1]

$$\frac{N^2 - 1}{12} = \frac{2\pi R^2}{\sigma}, \tag{A.10}$$

from which we deduce the steady state radius R that we seek

$$R = \sqrt{\frac{(N^2 - 1)\sigma}{24\pi}}. \tag{A.11}$$

This may be well approximated by the following linear dependence:

$$R \approx 0.115\sqrt{\sigma}N, \tag{A.12}$$

with less than 3% error for $N > 3$ and less than 1% for $N > 7$. We conclude that the equilibrium radius increases linearly with the particle size $\sqrt{\sigma}$ and the number of particles N.

[1] That led us to think that treating the odd and even case separately might not be necessary and that summing over all $N - 1$ particles directly might be possible.

Appendix B

Image system for simulations in a narrow channel

In this appendix, we explain how the non-penetration boundary condition at the walls of a narrow channel have been enforced in the numerical simulations described in Sec. 3.4.

To start with, Fig. B.1a shows how non-penetration modifies the flow generated by a swimmer in the vicinity of the wall. To be specific, let us consider a particle with orientation $\mathbf{p}$ located at y, at a distance δ from a confining wall as sketched in Fig. B.1b. Cancelling the normal component of the dipolar flow induced by its motion requires an image particle at the same distance on the other side of the wall $(y - 2\delta)$, with orientation $\mathbf{p}^* = (p_x, -p_y)$, i.e. with angle $-\theta$ (see Fig. B.1b). By doing that, we however induced a non-zero velocity through the virtual wall lying at $y = -W/2 - W$, which we cancel using the exact same strategy: we add an image of orientation $(\mathbf{p}^*)^* = \mathbf{p}$, located at $y - 2W$. Carrying out this method of reflection, we show that two distinct series of images are needed in the y direction:

- a set of *symmetric images* with orientation $\mathbf{p}^*$ at locations $y \pm 2nW - 2\delta$ (for physical particles located at $y < 0$, as in Fig. B.1a) or $y \pm 2nW + 2\delta$ (for $y > 0$),
- a set of *periodic images* with orientation $\mathbf{p}$ at locations $y \pm 2nW$.

In the x direction, the usual periodic boundary conditions appropriate for an infinitely long canal require the usual set of periodic images at locations $x \pm mL$ for each image introduced in y. The accelerated algorithm presented in Sec. 3.1 has been modified to implement this new type of boundary conditions. To compute the interaction due to particle j on particle i, we now not only compute directly the interaction due to the closest periodic image of j (vector $\mathbf{R}_{ij}^{min}$), but also the one due its closest symmetric image, which can potentially be very close to i if both i and j lie near the same wall (see Fig. B.1c). The far-field contributions due to all other particles is then approximated using a discrete Green tensor, whose pre-calculation at the beginning requires special care due to the combination of both types of images. Without entering into technical details, let us mention that a minimum of two discrete Green tensors are actually needed in that case.

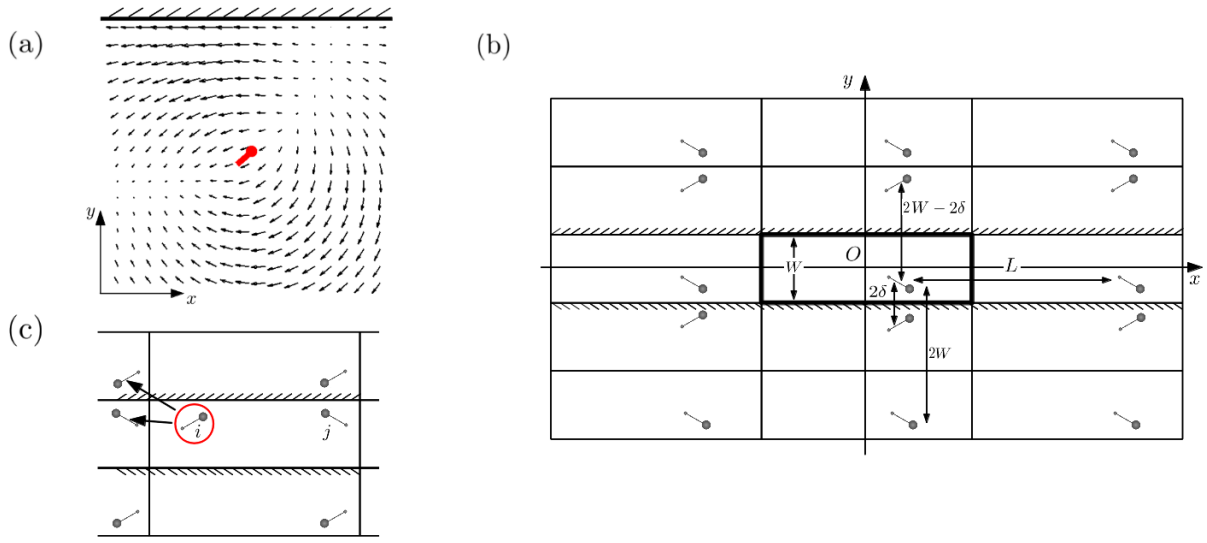

FIG. B.1: (a) Dipolar flow generated by a swimmer is modified near a wall to guarantee non-peneration (field computed from simulations). (b) Image system in a narrow channel of width W for a particle located at a distance δ of the lower wall. A series of periodic images at $y \pm 2nW$ and a series of symmetric images with appropriate orientation at $y \pm 2nW - 2\delta$ are included the y direction. In x, periodic images for all of these at $x \pm mL$ must be added. (c) Interactions at i due to the two closest images of j (periodic and symmetric) are directly computed.

Bibliography

[1] D. Saintillan, "Kinetic models for biologically active suspensions", in *Natural Locomotion in Fluids and on Surfaces: Swimming, Flying, and Sliding*, Springer (2012).

[2] D. Saintillan, M. J. Shelley, "Active suspensions and their nonlinear models", *C. R. Phys*, To appear (2013).

[3] D. Saintillan, M. J. Shelley, "Instabilities and pattern formation in active particle suspensions: Kinetic theory and continuum simulations", *Phys. Rev. Lett.* **100**, 178103 (2008).

[4] D. Saintillan, M. J. Shelley, "Instabilities, pattern formation, and mixing in active suspensions", *Phys. Fluids* **20**, 123304 (2008).

[5] D. Saintillan, M. J. Shelley, "Emergence of coherent structures and large-scale flows in motile suspensions", *J. R. Soc. Interface* **9**, 571-585 (2012).

[6] D. Saintillan, M. J. Shelley, "Orientational order and instabilities in suspensions of self-locomoting rods", *Phys. Rev. Lett.* **99**, 058102 (2007).

[7] A. Alizadeh Pahlavan, D. Saintillan, "Instability regimes in flowing suspensions of swimming microorganisms", *Phys. Fluids* **23**, 011901 (2011).

[8] D. Saintillan, "Extensional rheology of active suspensions", *Exp. Mech.* **50**, 1275 (2010).

[9] D. Saintillan, "The dilute rheology of swimming suspensions: A simple kinetic model", *Phys. Rev. E* **81**, 056307 (2010).

[10] A. Sokolov, I. S. Aranson, "Reduction of viscosity in suspensions of swimming bacteria", *Phys. Rev. Lett.* **103**, 148101 (2009).

[11] B. Ezhilan, A. Alizadeh Pahlavan, D. Saintillan, "Chaotic dynamics and oxygen transport in thin films of aerotactic bacteria", *Phys. Fluids* **24**, 091701 (2012).

[12] A. Sokolov, I. S. Aranson, J. O. Kessler, R. E. Goldstein, "Concentration dependence of the collective dynamics of swimming bacteria", *Phys. Rev. Lett.* **98**, 031903 (2007).

[13] B. Ezhilan, M. J. Shelley, D. Saintillan, "Instabilities and nonlinear dynamics of concentrated active suspensions", *Phys. Fluids*, To appear (2013).

[14] L. H. Cisneros, J. O. Kessler, S. Ganguly, R. E. Goldstein, "Instabilities and nonlinear dynamics of concentrated active suspensions", *Phys. Rev. E* **83**, 061907 (2011).

[15] J. S. Guasto, K. A. Johnson, J. P. Gollub, "Oscillatory Flows Induced by Microorganisms Swimming in Two Dimensions", *Phys. Rev. Lett.* **105**, 168102 (2010).

[16] T. Beatus, R. H. Bar-Ziv, T. Tlusty, "The physics of 2D microfluidic droplet ensembles", *Phys. Reports* **516**, 103-145 (2012).

[17] T. Beatus, T. Tlusty, R. Bar-Ziv, "Burgers shock waves and sound in a 2D microfluidic droplets ensemble", *Phys. Rev. Lett.* **103**, 114502 (2009).

[18] J. B. Caussin, "Dynamique des suspensions hors-équilibre confinées" (French), *ENS Lyon internship report* (2011).

[19] N. Desreumaux, J. B. Caussin, R. Jeanneret, E. Lauga, D. Bartolo, "Hydrodynamic fluctuations in confined emulsions", Submitted (2012).

[20] T. Brotto, J.-B. Caussin, E. Lauga, D. Bartolo, "Hydrodynamics of confined active fluids", *Phys. Rev. Lett.* **110**, 038101 (2013).

[21] E. M. Purcell, "Life at low Reynolds numbers", *Am. J. Phys.* **45**, 3-11 (1977).

[22] H. Diamant, "Hydrodynamic interactions in confined geometries", *J. Phys. Soc. Japan* **78**, 041002 (2009).

[23] S. E. Spagnolie, E. Lauga, "Hydrodynamics of self-propulsion near a boundary: predictions and accuracy of far-field approximations", *J. Fluid Mech.* **700**, 105-147 (2012).

[24] N. Liron, S. Mochon, "Stokes flow for a Stokeslet between two parallel flat plates", *J. Eng. Math.* **10**, 287-303 (1976).

[25] C. Pozrikidis, "Introduction to Theoretical and Computational Fluid Dynamics", Oxford University Press, 244 (1996).

[26] M. Garcia, B. Stefano, P. Peyla, S. Rafai, "Random walk of a swimmer in a low-Reynolds-number medium", *Phys. Rev. E* **83**, 035301 (2011).

[27] K. Drescher, J. Dunkel, L. H. Cisneros, S. Ganguly, R. E. Goldstein, "Fluid dynamics and noise in bacterial cell-cell and cell-surface scattering", *Proc. Natl. Acad. Sci. USA* **108**, 10940 (2011).

[28] H. Brenner,"A general theory of Taylor dispersion phenomena", *Physicochem. Hydrodyn.* **1**, 91-123 (1980).

[29] H. Brenner, "Taylor dispersion in systems of sedimenting nonspherical Brownian particles: I. Homogeneous, centrosymmetric, axisymmetric particles.", *J. Colloid Interface Sci.* **71**, 189-208 (1979).

[30] D. Saintillan, E. Darve, E. S. G. Shaqfeh, "A smooth particle-mesh Ewald algorithm for Stokes suspension simulations: The sedimentation of fibers", *Phys. Fluids* **17**, 033301 (2005).

[31] R. C. McOwen, "Partial Differential Equations: Methods and Applications" (Second Edition), Prentice Hall, 28 (2003).

[32] T. Nagatani, "The physics of traffic jams", *Rep. Prog. Phys.* **65**, 1331-1386 (2002).

[33] N. Sambelashvili, A. W. C. Lau, D. Cai, "Dynamics of bacterial flow: Emergence of spatiotemporal coherent structures", *Phys. Lett. A* **360**, 507 (2007).